

AD-A245 185



✓
①

CHARACTERIZATION OF MECHANICAL DAMAGE MECHANISMS IN CERAMIC AND POLYMERIC MATRIX COMPOSITE MATERIALS

By

James Lankford, Jr.

DTIC
ELECTE
JAN 29 1992
S D D

This document has been approved
for public release and sale; its
distribution is unlimited.

TECHNICAL REPORT
ONR Contract No. N00014-84-C-0213
ONR Contract Authority NR 032-553
SwRI-8124

For

Office of Naval Research
Arlington, VA 22217

By

Southwest Research Institute
San Antonio, Texas

92-01712



November 1991

Reproduction in whole or in part is permitted for any purpose of the United States Government



SOUTHWEST RESEARCH INSTITUTE
SAN ANTONIO
DETROIT
HOUSTON
WASHINGTON, DC

UNCLASSIFIED

SECURITY CLASSIFICATION OF THIS PAGE

REPORT DOCUMENTATION PAGE				Form Approved OMB No. 0704-0188 Exp. Date: Jun 30, 1986	
1a. REPORT SECURITY CLASSIFICATION Unclassified			1b. RESTRICTIVE MARKINGS		
2a. SECURITY CLASSIFICATION AUTHORITY			3. DISTRIBUTION/AVAILABILITY OF REPORT		
2b. DECLASSIFICATION/DOWNGRADING SCHEDULE			Dissemination Limited		
4. PERFORMING ORGANIZATION REPORT NUMBER(S) 06-8124			5. MONITORING ORGANIZATION REPORT NUMBER(S) NR 032-553		
6a. NAME OF PERFORMING ORGANIZATION Southwest Research Institute		6b. OFFICE SYMBOL (If applicable)	7a. NAME OF MONITORING ORGANIZATION Dr. Steven G. Fishman - code 431N Office of Naval Research		
6c. ADDRESS (City, State, and ZIP) 6220 Culebra Road, PO Drawer 28510 San Antonio, TX 78228-0510			7b. ADDRESS (City, State, and ZIP Code) 800 North Quincy Street Arlington, VA 22217		
8a. NAME OF FUNDING/SPONSORING ORGANIZATION Office of Naval Research		8b. OFFICE SYMBOL (If applicable)	9. PROCUREMENT INSTRUMENT IDENTIFICATION NUMBER N00014-84-C-0123		
8c. ADDRESS (City, State, and ZIP) 800 North Quincy Street Arlington, VA 22217			10. SOURCE OF FUNDING NUMBERS		
			PROGRAM ELEMENT NO.	PROJECT NO.	TASK NO.
					WORK UNIT ACCESSION NO.
11. TITLE (Include Security Classification) Characterization of Mechanical Damage Mechanisms in Ceramic and Polymeric Matrix Composite Materials					
12. PERSONAL AUTHOR(S) James Lankford					
13a. TYPE OF REPORT Technical		13.b TIME COVERED FROM 10/90 TO 10/91		14. DATE OF REPORT (Year, Month, Day) November 1991	
				15. PAGE COUNT 63	
16. SUPPLEMENTARY NOTATION					
17. COSATI CODES			18. SUBJECT TERMS (Continue on reverse if necessary and identify by block number)		
FIELD	GROUP	SUB-GROUP	Key Words: compressive strength, whisker-reinforced, composite materials; fracture mechanisms; ceramics; plasti flow		
			(aluminum oxides)		
19. ABSTRACT (Continue on reverse if necessary and identify by block number) (silicon carbides). The role of microplasticity in the compressive strength of strong ceramics is explored, emphasizing a representative oxide (Al_2O_3) and non-oxide (SiC). Relevant results from studies of hardness, compressive behavior, and impact response are considered. The combined evidence indicates that microplasticity is a vital factor in the compressive failure of even these very hard materials under essentially all conditions (temperature, strain rate, confinement). It is shown that uniaxial compressive strengths achieved under "perfect" test conditions approach one-third of the hardness as a limit. Under most conditions, dislocation activity appears to be detrimental to compressive strength. Since only an extremely limited number of slip systems is available for stresses below $H/3$, relaxation of intrinsic stress concentrators is ineffective; instead, the highly localized discrete slip bands themselves constitute intense grain boundary stress raisers, and thereby contribute significantly to prefailure compressive microfracture. Compressive failure of a $0^\circ/90^\circ$ glass fiber-reinforced amorphous thermoplastic is characterized. It is found that the critical event is the nucleation within 90° laminates of multiple shear crazes, which become shear microcracks, transition to axial cracks, and permit the specimen to fail by the flexure of 0° elements. Further, it is shown that the apparent kinetics of this process provide a rationale for the dramatic strain rate strengthening of these composites at high loading rate.					
20. DISTRIBUTION/AVAILABILITY OF ABSTRACT			21. ABSTRACT SECURITY CLASSIFICATION		
<input checked="" type="checkbox"/> UNCLASSIFIED/UNLIMITED <input type="checkbox"/> SAME AS RPT. <input type="checkbox"/> DTIC USERS			Unclassified		
22a. NAME OF RESPONSIBLE INDIVIDUAL James Lankford			22b. TELEPHONE (Include Area Code) 512/522-2317		22c. OFFICE SYMBOL

FOREWORD

This report describes recent work carried out under an experimental program aimed at characterizing damage mechanisms and compressive failure in ceramic and polymeric matrix composite materials. The report consists of two papers, each having been submitted for publication as noted on its title page.



Accession For	
NTIS CRASH	<input checked="" type="checkbox"/>
DTIC TAG	<input type="checkbox"/>
Unannounced	<input type="checkbox"/>
Justification	
By	
Dist to	
Available	
Dist	Special
A-1	

Statement A per telecon
Dr. Steven Fishman ONR/Code 1131
Arlington, VA 22217-5000
NWW 1/27/92

TABLE OF CONTENTS

	<u>Page</u>
The Compressive Strength of Strong Ceramics: Microplasticity Versus Microfracture	1
Abstract	1
1. Introduction	2
2. Hardness	3
3. Compressive Behavior	6
4. Impact Experiments	12
5. Discussion	13
6. Acknowledgements	17
7. References	17
Micromechanisms of Compressive Failure in a Glass Fiber-Reinforced Amorphous Thermoplastic	43
Abstract	43
Introduction	44
Material	44
Experimental Approach	45
Results	46
Discussion	48
Acknowledgements	51
References	51

LIST OF FIGURES

Figure		Page
The Compressive Strength of Strong Ceramics: Microplasticity Versus Microfracture		
1	Hardness versus temperature for high-purity alumina of various grain size.	22
2	Current optimum (MTL) compression test specimen design.	23
3	Compressive failure stress versus theoretical yield strength for strong ceramics using optimal uniaxial test configuration.	24
4	Compressive stress-strain curves for hot-pressed BeO.	25
5	Transmission electron microscopy of aluminum nitride.	26
6	Compressive failure stress versus theoretical yield strength for strong ceramics tested under confining pressure.	27
7	Hardness, theoretical yield strength, compressive failure stress, and tensile (bend) strength for coarse-grained ($\sim 30 \mu\text{m}$) 99.9% Al_2O_3 .	28
8	Hardness, theoretical yield strength, compressive failure stress, and tensile (bend) strength for fine-grained ($\sim 4 \mu\text{m}$) sintered alpha silicon carbide.	29
9	Compressive failure stress versus strain rate for coarse-grained high-purity alumina and fine-grained sintered alpha silicon carbide.	30
10	Axial microcracks nucleated by twin/deformation band interactions with grain boundary, Al_2O_3 , $T = 23^\circ\text{C}$.	31
11	High magnification view of early stages of craze breakdown via void nucleation to form shear crack; $\dot{\epsilon} \cong 4000\text{s}^{-1}$, $\sigma \cong 0.92 \sigma_c$; compressive axis vertical.	32
12	Grain boundary microfracture in Al_2O_3 caused by multiple twin impingement at $T = 500^\circ\text{C}$.	33
13	Dislocation slip bands (SB) in α -SiC induced by compression at $T = 500^\circ\text{C}$. Slip appears to have caused GB cracking at A and B and slip band cracking at C. The bands appear to initiate at GB pores.	34
14	Compressive strength versus inverse square root grain size of near-theoretical density high-purity Al_2O_3 .	35
15	Stress-microstrain during compressive load-unload for fully stabilized ZrO_2 (inset shows data for polycrystalline Cu).	36
16	Silicon carbide flyer plate experiment and prediction by one-dimensional Lagrangian shock wave propagation code incorporating elastic-plastic hardening constitutive behavior.	37
17	Geometry of compressive slip band-nucleated intracrystalline cleavage (1,2), intergranular separation (3), and slip band microfracture.	38
Micromechanisms of Compressive Failure in a Glass Fiber-Reinforced Amorphous Thermoplastic		
1	Configuration of compression test specimen.	53
2	Compressive stress and acoustic emission versus strain, $\dot{\epsilon} = 6 \times 10^{-6}\text{s}^{-1}$.	54

LIST OF FIGURES (Cont'd.)

Figure		Page
3	Stress level versus strain rate.	55
4	Macroscopic view of failed specimen, $\dot{\epsilon} = 1 \times 10^{-4} \text{s}^{-1}$, showing shear failure preceded by axial splitting.	56
5	Axial damage development; $\dot{\epsilon} = 1 \times 10^{-4} \text{s}^{-1}$, stress axis vertical, $\sigma = \sigma_c$.	57
6	Microcrack nucleation within 90° laminate; $\dot{\epsilon} = 1 \times 10^{-4} \text{s}^{-1}$, stress axis vertical, $\sigma \cong 0.95 \sigma_c$.	58
7	Linkup of shear microcracks within 90° laminate; $\dot{\epsilon} = 1 \times 10^{-4} \text{s}^{-1}$, stress axis vertical, $\sigma \cong 0.95 \sigma_c$.	59
8	Untested specimen (left) versus sample (right) tested at $\dot{\epsilon} = 4000 \text{s}^{-1}$ to a near failure stress level ($\sigma \cong 1500 \text{ MPa}$).	60
9	Dynamic shear crack nucleated in 90° laminate at $\dot{\epsilon} \cong 4000 \text{s}^{-1}$, $\sigma \cong 0.92 \sigma_c$, compressive axis vertical; crack has arrested (arrow) at 0° fiber interface.	61
10	Details of shear band shown in Figure 9.	62
11	Twin habit plane/deformation band cracking, Al_2O_3 , $T = 23^\circ\text{C}$.	63
12	Compressive strength versus strain rate for unidirectionally graphite fiber reinforced semicrystalline PEEK versus $0^\circ/90^\circ$ glass fiber reinforced amorphous thermoplastic.	64

**The Compressive Strength of Strong Ceramics:
Microplasticity Versus Microfracture**

J. Lankford

**Materials and Mechanics Department
Southwest Research Institute
6220 Culebra Road
San Antonio, Texas 78228-0510**

ABSTRACT *The role of microplasticity in the compressive strength of strong ceramics is explored, emphasizing a representative oxide (Al_2O_3) and non-oxide (SiC). Relevant results from studies of hardness, compressive behavior, and impact response are considered. The combined evidence indicates that microplasticity is a vital factor in the compressive failure of even these very hard materials under essentially all conditions (temperature, strain rate, confinement). It is shown that uniaxial compressive strengths achieved under "perfect" test conditions approach one-third of the hardness as a limit. Under most conditions, dislocation activity appears to be detrimental to compressive strength. Since only an extremely limited number of slip systems is available for stresses below $H/3$, relaxation of intrinsic stress concentrators is ineffective; instead, the highly localized discrete slip bands themselves constitute intense grain boundary stress raisers, and thereby contribute significantly to prefailure compressive microfracture.*

1. INTRODUCTION

The compressive failure of strong ceramics is a phenomenon which at first appearance may seem to reflect purely brittle fracture events. The process was described graphically by Dunlay, Tracy, and Perrone [1] in the course of reporting their important 1989 experiments as follows: "As the specimen was loaded along a seemingly elastic path, failure was an explosive event accompanied by a loud report and a flash of light (visible in a darkened room). The gage section and most of the tapered sections as well, were reduced to very fine rubble ranging in size from several millimeters to powder that took a good fraction of a minute to settle to the ground." This sounds brittle indeed.

In the following, however, it will be shown that there is every likelihood that plastic flow plays at least some role in the compressive failure of most strong ceramics under most conditions (i.e., temperatures and strain rates). As far back as 1971, in fact, Rice [2] surveyed exhaustively the then available literature on the compressive strength of ceramics, and came to the conclusion that microplastic yielding actually represents the upper limit of compressive strength. He suggested, in addition, that microplasticity probably plays an important role in compressive failure for very strong ceramics, even under conditions (such as low temperatures and high strain rates) generally thought to be dominated by brittle microfracture. At the time of these assertions, however, certain key types of experimental evidence which could provide powerful support for them were in short supply. Fortunately, this no longer is the case, particularly pertinent results having been obtained during the last decade. The purpose of this paper is to bring together and interpret this body of work, focussing on the relative roles of brittle microfracture and microplastic flow in the compressive failure of technological ceramics. Questions which will be addressed include: (1) Under what circumstances do ceramics experience plastic flow? (2) What are the consequences of such flow in terms of microfracture? (3) Are plastic flow considerations necessary in order to understand the compressive behavior of ceramics under nominally brittle circumstances? In order to answer these questions, several distinctly different experimental regimes will be explored, i.e., hardness, compression, and impact (flyer plate) testing.

It should be noted that since this paper is aimed at tying together such disparate factors, the decision was made to principally focus on two of the limited number of material systems for which most of the required information exists, namely, Al_2O_3 and SiC . Similar data are available for a few other ceramics such as MgO and LiF , but these generally fall into the "semi-brittle" classification. Alumina and silicon carbides, on the other hand, are considered archetype "brittle" materials.

In addition, no attempt has been made to treat all the factors which contribute to brittle compressive failure. In particular, there is no doubt that intrinsic geometric processing flaws nucleate a large fraction of the microcracks whose eventual coalescence constitutes compressive failure. Rice [2] has dealt with these issues, especially the crucial role of porosity, and twenty years later his treatment still is definitive. Likewise, the latter contains a comprehensive review of most earlier work in which a link between plasticity and fracture was sought or implicated.

2. HARDNESS

The issue of microplasticity in brittle materials is most directly addressed by appealing to indentation testing. For example, it has been known for decades that the hardness of brittle materials, like that of metals, is extremely temperature dependent [3-11]. This is true even for the low homologous temperature regime, $T < 0.5T_{\text{MP}}$, within which grain boundary sliding processes are known to be precluded [10]. The various thermally activated mechanisms that have been postulated to explain this behavior thus have all been based on dislocation concepts.

Justification for this approach is easily obtained by comparing the hardness (H) versus temperature (T) trends obtained for polycrystalline and single crystal variants of the same ceramic. Shown in Figure 1 are such data [9] for Al_2O_3 , in which one observes that for both single crystal sapphire and polycrystalline, 99.9% alumina of two widely differing grain sizes, $H(T)$ dependencies are virtually identical. Since the single crystal, lacking grain boundaries, can deform only by dislocation activity, it is evident that this must be responsible for the observed trend. Moreover,

the equivalent single crystal/polycrystalline hardness values suggest that for each temperature, the physical nature of the deformation beneath the indentation is not altered by the presence or absence of grain boundaries.

Similar results have been reported [5] for SiC, differing slightly in the lack of coincidence of polycrystalline and single crystal $H(T)$ data. However, the data obey similar functions, and multi-system intracrystalline dislocation activity again is inferred.

It has now been directly established by transmission electron microscopy (TEM) that multiple slip system dislocation activity is directly responsible for permanent indentations in strong ceramics. Particularly convincing are the observations of Hockey and his colleagues [12,13]. For example, extensive TEM evidence of both slip and twinning at room-temperature indentations was first observed [12] in Al_2O_3 . Near the indenter-crystal contact point, the density of dislocations was so great that individual dislocations could not be resolved. Both basal and nonbasal slip and microtwin systems were observed. Verification of similar prolific plastic flow associated with room temperature indentations was subsequently obtained for other "brittle" ceramics, including Si, Ge, and SiC [13].

A particularly prescient question was posed by Hockey at the conclusion of his 1971 paper [12], i.e., "whether dislocations introduced by abrasion or indentation are associated with the initiation or propagation of cracks." That cracks are generated at the sites of indentations in brittle solids is the basis for the current development of the field of indentation fracture analysis [14], which capitalizes on the (apparently) truly brittle fracture associated with the growth of the cracks. Recent attention, however, has focussed on the combined deformation-fracture zone associated with indentations in sapphire. Thus, Chan and Lawn [15] discovered, via TEM, that both basal twinning and pyramidal slip are primarily responsible for severe shear faulting beneath indentations in Al_2O_3 . Moreover, associated with both twin interfaces and slip planes are incipient

microcracks, which act as nucleation sites for both radial and lateral indentation cracks. It is clear that this is so, since the radials and laterals generally deviate from crystallographic, low index apparent nucleation planes as they move away from the indentation.

Swain [16] has shown that dislocations introduced during abrasive wear (a variant of indentation testing) can cause cracking by a different mechanism. In particular, the track of a Vickers indenter which had been drawn across an alumina surface was etched to reveal slip lines within individual grains. Extensive grain boundary cracking was observed along the "wear track," but only adjacent to regions where slip bands interacted with the grain boundaries. Specifically, stresses apparently associated with the heads of dislocation pileups blocked by grain boundaries were relaxed by the nucleation of classic Zener-Stroh [17,18] intergranular cracks.

The factor which permits the abundant plastic flow associated with an indentation is the intense confining pressure induced within the elastic surround. Hill [19] and Tabor [20] have analyzed the indentation process to show that for ductile metals, the hardness (indentation pressure) H is related to the yield strength Y by

$$Y = H/3 \quad (1)$$

This means [4] that two-thirds of the pressure beneath the indenter is hydrostatic, and one third is shear stress, only the latter inducing plastic flow. Tabor [21] has shown that the above relationship is well-obeyed for many metals. The latter actually is a limiting case of analytical treatments of indentation deformation which take into account elastic as well as plastic strain accommodations. This situation is discussed in detail in the Appendix, where it is shown that in general $Y = H/C$, where C , the constraint factor, can vary from a low of 1.1 (purely elastic behavior) to a high of about 3 (perfectly plastic indentation). In the present context, $C = 3$ will be used, since: (1) it is a consistent, useful, and probably realistic [2] figure-of-merit for the yield strength of ceramics; (2) the current analytical treatments, which predict a slightly lower value, are only theories, with their own assumptions (isotropic behavior, specific yield criteria); and (3) $Y = H/3$ represents the

theoretically lowest possible general (multi-slip) yield stress for a ceramic, thus it is the absolute lowest stress at which there is a chance for achieving macroscopic yielding in a uniaxial compression test.

3. COMPRESSIVE BEHAVIOR

Measurement of the true compressive strength of a brittle material is a difficult undertaking. As noted by Rice [2], parasitic stresses, which compromise the ability of the material to manifest its highest intrinsic strength, may arise from several sources. These principally include misalignment (nonparallelism) of the specimen-platen interfaces, which produce bending (tensile) failure, and interface effects, caused by friction and non-matching Poisson expansion between specimen and interface. Misalignment problems can be mitigated by careful specimen/platen machining and pretest alignment procedures, while the interface itself can be more-or-less removed from the problem by utilizing a reduced section specimen. For rocks, the strength reduction associated with a simple right circular cylinder versus a reduced-section circular cross-section can be as large as 30% [22]. Moreover, just as the stress distribution in a "uniaxially" loaded right circular cylinder is actually triaxial [23], finite element analysis has shown [1] that even the current best reduced section specimen design [1] incorporates localized stresses, fortunately low level, that perturb the "uniaxial" applied stress field.

Using the latter specimen design (Figure 2), combined with extremely painstaking alignment procedures, Dunlay, et al. [1], recently performed probably the most perfect compression tests yet reported for strong ceramics. The results are shown in Figure 3, as compressive strength σ_c versus H/c , the theoretical yield strength. Although only for the case of alumina was the theoretical yield strength attained, it was nearly reached for TiB_2 and hot-pressed SiC. Since the specimens apparently were not strain-gaged, no evidence of the presence or absence of stress-strain nonlinearity is available. However, it seems noteworthy that the strength of no material was sufficient to exceed σ_c versus H/c . The principal difference between the two silicon carbides was that for the hot-pressed version, porosity was drastically reduced. The observed disparity in σ_c therefore is in

accord with the general influence of porosity documented earlier by Rice [2]. As reported elsewhere [24], the author has measured a quasistatic (strain rate) compressive strength of approximately 4.0 GPa for the sintered SiC, which compares with the average value of 4.55 GPa reported by Dunlay, et al. This difference probably derives from the two specimen configurations used, i.e., simple right circular cylinder compressed by alumina platens of the same configuration [24], versus reduced section cylinder [1].

It has by now been firmly established that brittle materials, ranging from rocks to the strongest ceramics, fail under compressive loading by a process of axial microcrack nucleation, growth, and coalescence [24-31]. Study of the volumetric dilatation [29,31] and acoustic emission [24,30] associated with the onset and development of compressive damage indicates that crack nucleation begins at an early stage, generally at stress levels no higher than about one-half the compressive strength. A powerful means of controlling crack development is the application of confining pressure, which has been shown (for rocks in particular [31]) to dramatically increase compressive strength.

In an important 1980 paper, Heard and Cline [32] reported on compression experiments performed under radial confinement to pressures (P) as high as 1.25 GPa for Al_2O_3 , AlN , and BeO . Typical stress-strain results are shown in Figure 4 for beryllium oxide; the stress plotted on the vertical scale is the axial stress deviation from the hydrostat required to fail the specimen. At the lowest pressures, the material is essentially elastic to failure, which occurs by macroscopic shear on fault planes oriented at about 30° to the axis, while the bulk of the unfailed material is riddled with axial microcracks [33]. As P increases from 0.1 to 0.5 GPa, post yield strain increases due to plastic flow preceding the failure. Although local fracturing occurs initially, this is suppressed as the pressure rises, i.e., the material undergoes a brittle-ductile transition at $P \geq 0.5$ GPa, and the ceramic subsequently hardens stably. At the highest pressure, the dominant deformation mechanism, as determined by TEM, is intracrystalline slip by dislocation motion, with attendant pile-up at grain boundaries. Aluminum nitride behaves similarly, while the failure of aluminum oxide is elastic to the highest attainable pressure, 1.25 GPa. An example of plastic deformation induced by

compression in AlN at high confining pressure is shown in Figure 5b, compared with the initial defect free state (Figure 5a). Dislocation activity is intense parallel to the traces of all three a-axes, indicating multi-slip system activity.

Figure 6 shows the results of Heard and Cline [32], plotted in the same format as Figure 3. Here it can be seen that BeO and AlN, under confinement, fail in a brittle manner until the compressive stress slightly exceeds the theoretical yield strength. Subsequent failure at any stress level in excess of this is plastic flow induced. Likewise, it is now evident why Heard and Cline [32] observed only elastic behavior for Al_2O_3 , i.e., the load capacity of their pressure bomb was incapable of providing the microcracking restraint (hydrostatic pressure) necessary for σ_c to exceed H/c .

The question still remains as to the possible influence of microplasticity in the strength regime $\sigma_c < H/c$. However, compression experiments performed by Lankford [24-26,30,34-39] as a function of temperature and strain rate, provide some insight regarding this point. Figures 7 and 8 for example, show the compressive strength of high purity polycrystalline alumina and sintered silicon carbide over a wide range in temperature at a strain rate of about $1 \times 10^{-4} \text{ s}^{-1}$. Also shown for comparison are hardness and tensile (bend) strength (σ_T) for virtually identical material. Strain rates for the bend tests were similar to those in the compression work, while the strain rates in the 15-second hardness tests are calculated to be $5.5 \times 10^{-3} \text{ s}^{-1}$, based on the estimate of 0.08 for the total plastic strain associated with an indentation [4]. For both materials, the temperature range shown in the figures lies below $0.5T_{MP}$, hence, grain boundary sliding is not considered a potential deformation mechanism.

By operating on the hardness data to generate $H/c(T)$, it is possible to compare the behavior of σ_c with both a plastic flow-dominated function (H/c), as well as one (σ_T) governed by thermally-activated microcrack growth [42,43]. It is generally believed that the latter is not controlled by dislocation activity, but rather classic thermal-activation of crack tip interatomic bonding.

In Figure 7, the close correlation in the decreases observed in H/C and σ_C from $T \cong 400^\circ\text{C}$ to 1000°C is striking; concurrently, σ_T is almost constant. Moreover, H/C is only about 50% greater than σ_C over this range, and since it has been shown that hardness reflects multi-slip system activity, this suggests that compressive activation of preferred slip systems should be relatively easy. Based on these considerations, it seems likely that plasticity-induced damage is responsible for the observed compressive strength degradation at intermediate temperatures. It will be shown shortly that microscopic evidence supports this conclusion.

For temperatures below 400°C , the situation seemingly is less clear in that σ_C , H/C , and σ_T all decrease with temperature (until σ_C suddenly increases at around 200°C). However, consideration of the strain rate ($\dot{\epsilon}$) dependence of σ_C provides insight as to the basis for this effect. Thus, as shown in Figure 9 for experiments performed at 23°C , σ_C versus $\dot{\epsilon}$ is well described by

$$\sigma_C \propto \dot{\epsilon}^{1/53} \quad (2)$$

which is the relationship predicted based on the kinetics of thermally activated crack growth. In this case, the results are described in terms of

$$\sigma_C \propto \dot{\epsilon}^{1/1+n_C} \quad (3)$$

analogous to the tensile strength relationship

$$\sigma_C \propto \dot{\epsilon}^{1/1+n_T} \quad (4)$$

where n_C and n_T are constants. Experiments have shown [44-46] that $n_T \approx n$, the experiment in the fracture mechanics relationship

$$V = AK^n \quad (5)$$

where V is the growth velocity of a subcritical Mode I tensile crack in a fracture mechanics specimen subject to a stress intensity K (A is a constant). For the alumina of Figure 9 (and 7 as

well), $n = 52$ [42]; the assumption that $n_c = n$ yields Equation (2). Thus, despite the thermally activated, microplastic sensitivity of H at low homologous temperatures, the implication here is that the temperature-strain rate dependence of σ_c within this range is controlled by the subcritical growth of microcracks.

On the other hand, there exists clear evidence that microplasticity does play a major role in compressive failure within this same regime. Shown in Figure 10 are twins and/or dislocation bands, formed during ambient compression to $0.85 \sigma_c$, that have nucleated axial microcracks (compressive stress is vertical) where the twins/bands have intersected a grain boundary. It is evident that cracks have formed within both the grain containing the deformation bands, as well as the adjacent grain, and it appears that the grain boundary itself may have cracked. In another grain (Figure 11), several microcracks have nucleated within the twin habit or slip band planes. Finally, grain boundary separation has been induced at 500°C by the impingement of apparent multiple twins, which appear to have wedged open the boundary (Figure 12). Reconciliation of these observations with the concurrent influence of thermally activated microcrack growth will be developed in the Discussion.

A similar scenario, differing only in its details, seems to hold for SiC as well. As shown in Figure 8, the decline of $H/c(T)$ and $\sigma_c(T)$ at temperatures greater than $\sim 300^\circ\text{C}$ and 550°C , respectively, is counter to the gradual and monotonic increase of $\sigma_T(T)$. Again, it appears that σ_c probably is controlled by plastic flow within this regime.

At lower temperatures, H/c is basically independent of temperature, while the rate of increase in σ_T with T is matched by that of σ_c . This behavior suggests that again, low homologous temperature compressive strength kinetics may be a function primarily of microcrack growth. From Figure 9, it is evident that ambient temperature $\sigma_c(\dot{\epsilon})$ data are well fit by a relationship of the form

$$\sigma_c \propto \dot{\epsilon}^{1/201} \quad (6)$$

which is predicted on the basis that $n_c = n \cong 200$ [43].

Although SEM search for evidence of compressive deformation was inconclusive for ambient temperature tests, this was not the case for somewhat higher temperatures. At 500°C (Figure 13), there was extensive evidence of slip bands (SB), which often appeared to nucleate grain boundary failure (A, B). At other sites, cracking of slip bands themselves was observed (C). In most cases, grain boundary pores constituted the microcrack nuclei.

One of the major accomplishments of the earlier work by Rice [2] was the compiling of a massive amount of evidence indicating the effect of grain size on compressive strength, whereby an inverse square root grain size relationship was identified for a wide variety of ceramics over a broad range in temperature. Petch relationships of this sort are almost invariably associated with plastic flow, and cannot be interpreted in terms of subcritical crack growth. The plot shown in Figure 14 shows Petch-type behavior for high purity Al_2O_3 [2] (equivalent data are unavailable for SiC); the implications of this result in the present context are developed in the Discussion.

A final related point which should be considered in the issue of plastic anisotropy. Earlier work has shown that for ceramic single crystal compression tests performed at fairly high temperatures, the ratio of the measured yield strength to the critical resolved shear stress (CRSS) on the primary slip system may be extremely high. Westbrook [47], for example, found that for rocksalt-structured ceramics, this ratio may be as high as 30.

Even more pertinent to the present focus on strong ceramics is the ambient deformation behavior of zirconia crystals reported by Lankford [48]. The material was characterized by Ingel [49], who found it to be free of impurities and porosity, and virtually theoretically dense; the material tested was composed of untransformable, fully-stabilized cubic phase. When compressed along $\langle 123 \rangle$ under quasistatic, ambient conditions, specimens exhibited the stress-strain response shown in Figure 15. Yielding, which occurs at a stress level of about 860 MPa, is followed by stable hardening; upon unloading, a period of inelastic recovery is followed by elastic relaxation, and finally reverse plastic flow occurs near zero load. As shown in the inset, precisely the same qualitative behavior occurs in the case of copper [50], and can only be explained in terms of dis-

location concepts. Since for this zirconia $H = 16.0$ GPa [49], the theoretical yield strength is estimated to be 5.33 GPa, approximately 6.2 times greater than the critical stress (860 MPa) for microyielding. Thus, polycrystalline plastic flow would be anticipated to occur within sufficiently large $\langle 123 \rangle$ oriented grains at compressive stress levels well below H/C .

On the other hand, a similar, but randomly oriented crystal was loaded to a failure stress of 2300 MPa along a totally elastic path. Clearly, plastic flow in this representative strong oxide is highly anisotropic.

4. IMPACT EXPERIMENTS

Flyer plate, or ceramic against ceramic high velocity impact experiments, are in essence a special case of compression testing. In particular, the loading rate is so rapid that strain is one dimensional, i.e., the impacting flyer and stationary target shorten in the direction of the impact, but because the event occurs so suddenly, the material inertia of the specimens effectively subjects them to total confinement.

Because of the high impact velocities, extremely rapid strain rates (on the order of 10^5 s^{-1}) and high compressive stresses are generated. The latter are sufficient to cause the material to apparently yield, as manifested in a change in the velocity of the shock waves introduced into the body. This point is known as the Hugoniot elastic limit (HEL), at which stress level the inertial confining pressure for ceramics is generally found to be on the order of $H^{HEL}/2$. The interpretation of this "yield" phenomenon in ceramics has been controversial, with suggested rationale including microcracking, phase transformation, and dislocation activity [51-56]. Recently, there has been considerable progress in discriminating between these possibilities, and a consensus seems to be emerging, at least for alumina and silicon carbide.

In the case of high purity Al_2O_3 , measured HEL values for sintered and hot-pressed versions are 11.2 GPa and 13.4 GPa, respectively [53]. These compare with an equivalent hardness-based quasistatic ($\dot{\epsilon} \approx 10^{-2} \text{ s}^{-1}$) yield strength of 6.7 GPa [9], and would appear to reflect strain-rate hard-

ening. Transmission electron microscopy and X-ray study of shocked specimens has shown [54] that dislocation deformation is present from below the HEL to stress levels twice its value. This leads Longy and Cagnoux [54] to conclude that the HEL represents the microplastic-to-macroplastic threshold. Louro and Meyers [55] performed similar shock experiments at stress levels maintained below the HEL; they, too, observed dislocations associated with the onset of damage.

Kipp and Grady [56] have arrived at a similar conclusion with regard to SiC, but by a somewhat different line of reasoning. Shown in Figure 16 is the time-profile of the target interface velocity for a SiC flyer impacting a SiC target. The stress level at which the velocity-time relationship deviates from elastic linearity is identified as the HEL, above which the velocity-time slope is lower, indicating the operation of a dispersive mechanism. Initial unloading is elastic (non-dispersive) which implies the full retention of yield strength by the SiC during and after unloading.

It is not surprising, therefore, that the experimental results are accommodated so well (Figure 16) by means of a simple classic plastic flow model. In this case, Herrmann's strain hardening model [57], originally devised to account for metal plasticity, is incorporated into a one-dimensional explicit Lagrangian shock wave propagation code [58]. A critical factor in the excellent agreement between this plastic flow-based theory and the actual velocity-time profile is the necessity of including within the calculation a late-time tensile fracture strength of 50 MPa. The overall conclusion is that the dynamic compression of SiC is dominated by plastic flow, if constraint (inertial, in this case) is sufficient to inhibit microfracture. As was the case for alumina, the HEL for SiC (~ 15.1 GPa) significantly exceeds the quasistatic yield strength, $H/c = 6.7$ GPa, again implicating rate dependent deformation processes.

5. DISCUSSION

Based on the foregoing, it is possible to try to answer the questions posed at several points throughout the paper. Thus, it appears reasonable to conclude that strong ceramics like Al_2O_3 and

SiC do experience multi-slip system plastic flow under compressive loading if the yield point can be attained, i.e., if the specimen does not fracture during the attempt. Generally, some type of hydrostatic confinement to inhibit flaw-nucleated microcrack development is necessary in order to accomplish the latter. At low strain rates, the stress level required for macroscopic plastic flow is approximately $H/3$, while under dynamic loading, it is necessary to reach the Hugoniot elastic limit. Moreover, based on the experience of Dunlay, et al. [1], it may well be possible to reach the plastic limit in a "perfect" uniaxial (unconfined) compression test, if the ceramic is sufficiently flaw (pore) free.

However, it probably would not be possible to exceed Y in such a test, because the effect of plastic flow under these conditions appears to be detrimental. As demonstrated in Figures 10-13, dislocations and twins induced by compression tend to nucleate microcracks. This is strongly supported by the intermediate temperature $\sigma_c(T)$ behavior of both Al_2O_3 and SiC, which closely parallels the decline in H with increasing T ; the latter is a consequence of dislocation activity [5]. Microcracks nucleated by the latter evidently are responsible for the observed $\sigma_c(T)$ dependence. Moreover, it is highly likely that dislocation- (and twin) induced microfracture is an important factor in apparent "brittle" compressive failure at lower temperatures, in which regime it already has been argued that microcrack kinetics, not thermally activated plasticity, account for the observed strength-strain rate dependence. This apparent conflict can be rationalized by considering the origin of the microcracks.

First, the experimental findings marshalled by Rice [2] demonstrating the inverse square root grain size dependence of ambient compressive strength constitute compelling circumstantial evidence pointing to the probable influence of plasticity in microcrack nucleation. In addition, one recalls the ambient compressive slip/twin nucleated microcracks observed in Al_2O_3 (Figures 10 and 11), and the room temperature anisotropic plasticity of compressed single crystal ZrO_2 (Figure 15). These factors suggest that the crux of the issue is the development of microcracks at preferential plastic enclaves within an otherwise elastic surround, a problem which can be treated in terms of the Zener-Stroh formalism as follows [17].

The critical value of the resolved shear stress on an operable slip plane at the tip of which a crack will nucleate is expressed by

$$\tau_{\text{crit}} = \left\{ \frac{\pi \gamma G f(\phi)}{2(1-\nu)d} \right\}^{1/2} \quad (7)$$

where γ is the surface energy associated with the crack; G is the shear modulus; f is a geometrical function of ϕ , the angle subtended by the slip plane and the projected crack (Figure 17); ν is Poisson's ratio; d is the dislocation pileup length (related to the characteristic size of the grain); and a is the as-nucleated length of the crack. Since it can be observed in Figure 17 that a variety of crack types may be nucleated, γ will represent either the surface energy for preferential intracrystalline cleavage (1,2), the grain boundary surface energy (3), or the surface energy associated with slip plane cleavage (4). Which mode of cracking is observed in a given case will depend on the combination of slip band, grain boundary, and potential cleavage plane orientations.

For ductile materials, at a certain pileup length cross-slip and/or dislocation climb will occur, and nearby parallel slip bands will be activated. In the case of ceramics, it is known that the Peierls barrier to dislocation motion is high and anisotropic (recall the discussion attending Figure 15); both climb (under ambient conditions) and secondary slip system activity will be difficult. In consequence, the operation of dislocation systems in strong ceramics is not likely to be a strong function of thermal activation factors. That is, temperature-induced changes in the Peierls stress field, the local barrier to dislocation motion, probably are insignificant compared to the high average stress required to move a dislocation through the field, especially for secondary slip systems. This explains why the only thermally-activated processes manifest in low-temperature compressive behavior are non-dislocation ones associated with microcrack growth.

It thus appears that dislocations within the most favorable system are likely to be confined there, where they must, as the pileup lengthens, either (1) block the source of slip; (2) create a microcrack at the head of the pileup; or (3) nucleate slip in the grain adjacent. The extremely

limited slip-system possibilities render the latter unlikely. Ultimately, the competition between source blockage and microfracture will be controlled by grain size. From Equation (7), it is obvious that τ_{crit} is minimized when d is large, and large pileups are in turn favored by large grain size. The shear stress at the head of a pileup of n dislocations generated by a shear stress (τ_s) at the source is approximately $n\tau_s$, so that for very large grains, n can increase more-or-less indefinitely until fracture occurs. Conversely, for small grains, a point can be reached at which the back stress from the non-critical (for crack nucleation) pileup is sufficient to block the dislocation source, so that no fracture can occur. This would appear to be responsible for the observed [2] trends in compressive strength versus grain size.

Contrasting with the near athermal, minimum slip system picture for compression, the robust $H(T)$ dependence observed for many materials [3-11] at low homologous temperatures does reflect the influence of thermal activation. Alumina, in the present context, exemplifies this type of behavior (Figure 7) in particular. Beneath an indenter, the stress level is sufficient to activate nearly all the available slip systems. The competition between actively competing mechanisms at such high overall stresses is sensitive to the influence of temperature and strain rate, which directly control obstacle-avoidance mechanisms such as cross slip, climb, and secondary slip system operations in general.

In conclusion, it appears that plastic flow considerations indeed are a necessary component to understanding the compressive behavior of ceramics like Al_2O_3 and SiC. Moreover, plasticity generally has a negative influence, in that the available slip systems are not only too limited to permit the relaxation of crack-nucleating flows (such as pores), but in fact dislocation activation necessarily contributes its own population of microcracks to the intrinsic flaw-generated crack ensemble.

6. ACKNOWLEDGEMENTS

The author is grateful for the support of the Office of Naval Research, under whose auspices his own work in the subject of compression of ceramics began. He also is grateful to R. W. Rice for his early, and continued, advice and encouragement.

7. REFERENCES

1. W. A. Dunlay, C. A. Tracy, and P. J. Perrone, "A Proposed Uniaxial Compression Test for High Strength Ceramics," U. S. Army Materials Technology Laboratory MTL TR 89-89 (September 1989).
2. R. W. Rice, "Ceramics in Severe Environments," *Mat. Sci. Res.*, 5, (W. W. Kriegel and H. Palmer, ed.), Plenum Press, NY, pp. 195-227 (1971).
3. R. D. Koester and D. P. Moak, *J. Am. Ceram. Soc.*, 55, pp. 290-296 (1967).
4. D. L. Kohlstedt, *J. Mat. Sci.*, 8, pp. 777-786 (1973).
5. M. G. S. Naylor and T. F. Page, Proc. Fifth Int. Conf. on Erosion by Liquid and Solid Impact, Cavendish Laboratory, Cambridge, 32, pp. 1-10 (1979).
6. A. G. Atkins and D. Tabor, *Proc. Roy. Soc. A*, 292, pp. 441-459 (1966).
7. B. Evans and C. Goetze, *J. Geophys. Res.*, 84, pp. 5505-5524 (1979).
8. J. H. Westbrook, *Rev. Hautes Temper. et Refract.*, 3, pp. 47-57 (1966).
9. C. P. Alpert, H. M. Chan, S. J. Bennison, and B. R. Lawn, *J. Am. Ceram. Soc.*, 71, pp. C371-C373 (1988).
10. A. Kvell and O. V. Bakun, *Acta Metall.*, 34, pp. 1315-1319 (1986).
11. W. Kollenberg, *J. Mat. Sci.*, 23, pp. 3321-3325 (1988).

12. B. J. Hockey, *J. Am. Ceram. Soc.*, 54, pp. 223-231 (1971).
13. B. R. Lawn, B. J. Hockey, and S. M. Wiederhorn, *J. Mat. Sci.*, 15, pp. 1207-1223 (1980).
14. R. F. Cook and G. M. Pharr, *J. Am. Ceram. Soc.*, 73, pp. 787-817 (1990).
15. H. M. Chan and B. R. Lawn, *J. Am. Ceram. Soc.*, 71, pp. 29-35 (1988).
16. M. V. Swain, *Wear*, 35, pp. 185-189 (1975).
17. D. Krajcinovic and A. Stojimirovic, *Int. J. Frac.*, 42, pp. 73-86 (1990).
18. A. Cottrell, *Trans. Met. Soc. AIME*, 208, pp. 192-203 (1958).
19. R. Hill, "The Mathematical Theory of Plasticity," Clarendon Press, Oxford (1950).
20. D. Tabor, "The Hardness of Metals," Clarendon Press, Oxford (1951).
21. D. Tabor, *Rev. Phys. Tech.*, 1, pp. 145 (1970).
22. W. F. Brace, "State of Stress in the Earth's Crust," W. R. Judd, ed., Elsevier, N.Y. pp. 111-174 (1964).
23. S. D. Peng, *Int. J. Rock. Mech. Min. Sci.*, 8, pp. 399-432 (1971).
24. J. Lankford, *J. Am. Ceram. Soc.*, 62, pp. 310-312 (1979).
25. J. Lankford, *J. Mat. Sci.*, 12, pp. 791-796 (1977).
26. J. Lankford, Proc. Third Int. Conf. Frac. Mech. Ceram., R. C. Bradt, A. G. Evans, D.P.H. Hasselman, and F. F. Lange, eds., Plenum Press, NY, pp. 625-637 (1983).
27. W. F. Brace and E. G. Bombolakis, *J. Geophys. Res.*, 68, pp. 3709-3713 (1963).
28. T. N. Dey and C.-Y. Wang, *Int. J. Rock Mech. Min. Sci. & Geomech. Abstr.*, 18, pp. 199-209 (1981).

29. P. Tapponier and W. F. Brace, *Int. J. Rock Mech. Min. Sci. & Geomech. Abstr.*, 13, pp. 103-112 (1976).
30. J. Lankford, *J. Mat. Sci.*, 16, pp. 1567-1578 (1981).
31. W. F. Brace, B. Paulding, and H. Scholz, *J. Geophys. Res.*, 71, pp. 3939-3954 (1966).
32. H. C. Heard and C. F. Cline, *J. Mat. Sci.*, 15, pp. 1889-1897 (1980).
33. J. Lankford, unpublished research on Al_2O_3 (1990).
34. R. J. Charles, "Studies of the Brittle Behavior of Ceramic Materials," ASD-TR-61-628, pp. 467 (1963).
35. D. C. Larsen and J. W. Adams, "Property Screening and Evaluation of Ceramic Turbine Materials," IITRI Technical Report No. 8, AFWAL F33615-79-C-5100 (June 1980).
36. J. Lankford, *Int. J. Rock Mech. Min. Sci. & Geomech. Abstr.*, 18, pp. 173-175 (1981).
37. J. Lankford and D. L. Davidson, Proc. Third Int. Conf. Mech. Behavior Mats., 3, K. J. Miller and R. F. Smith, eds., Pergamon Press, NY, pp. 35-43 (1980).
38. J. Lankford, *J. Am. Ceram. Soc.*, 64, pp. C33-C34 (1981).
39. J. Lankford, *J. Am. Ceram. Soc.*, 65, pp. C122 (1982).
40. J. Lankford, *J. Mat. Sci.*, 18, pp. 1666-1674 (1983).
41. J. Lankford, *J. Mat. Sci.*, 8, pp. 947-949 (1989).
42. A. G. Evans, M. Linzer, and L. R. Russell, *Mat. Sci. Eng.*, 15, pp. 253-261 (1974).
43. K. D. McHenry, T. M. Yonushonis, and R. E. Tressler, *J. Am. Ceram. Soc.*, 59, pp. 262-263 (1976).

44. A. G. Evans, *J. Mat. Sci.*, 7, pp. 1137-1146 (1972).
45. A. G. Evans and H. Johnson, 10, pp. 214-222 (1975).
46. A. G. Evans, *Int. J. Fract.*, 10, pp. 251-259 (1974).
47. J. H. Westbrook, *J. Amer. Ceram. Soc.*, 41, pp. 433-440 (1958).
48. J. Lankford, *J. Mat. Sci. Ltrs.*, 8, pp. 947-949 (1989).
49. R. P. Ingel, "Structure-Mechanical Property Relationships for Single Crystal Yttrium Oxide Stabilized Zirconium Oxide," PhD Thesis, Catholic University of America (1982).
50. A. R. Rosenfield and B. L. Averbach, *Acta Metall.*, 10, pp. 71-74 (1962).
51. D. E. Munson and R. J. Lawrence, *J. Appl. Phys.*, 50, pp. 6272-6282 (1979).
52. W. H. Gust, A. C. Holt, and E. B. Royce, *J. Appl. Phys.*, 44, pp. 550-560 (1973).
53. W. H. Gust and E. B. Royce, *J. Appl. Phys.*, 42, pp. 276-294 (1971).
54. F. Longy and J. Cagnoux, *J. Am. Ceram. Soc.*, 72, pp. 971-979 (1989).
55. L. H. L. Louro and M. A. Meyers, *J. Mat. Sci.*, 24, pp. 2516-2532 (1989).
56. M. E. Kipp and D. E. Grady, "Shock Compression and Release in High-Strength Ceramics," Sandia National Laboratories Report SAND89-1461-UC-704 (July 1989).
57. W. Herrmann, R. J. Lawrence, and D. S. Mason, "Strain Hardening and Strain Rate in One-Dimensional Wave Propagation Calculations," Sandia National Laboratories Report SC-RR-70-471 (November 1970).
58. M. E. Kipp and R. J. Lawrence, "WONDY V-A One Dimensional Finite Difference Wave Propagation Code," Sandia National Laboratories Report SAND81-0930 (June 1982).

59. D. M. Marsh, *Proc. Roy. Soc. (London)*, 279A, pp. 420-435 (1964).
60. K. Johnson, *J. Mech. Phys. Solids*, 18, pp. 115-126 (1970).

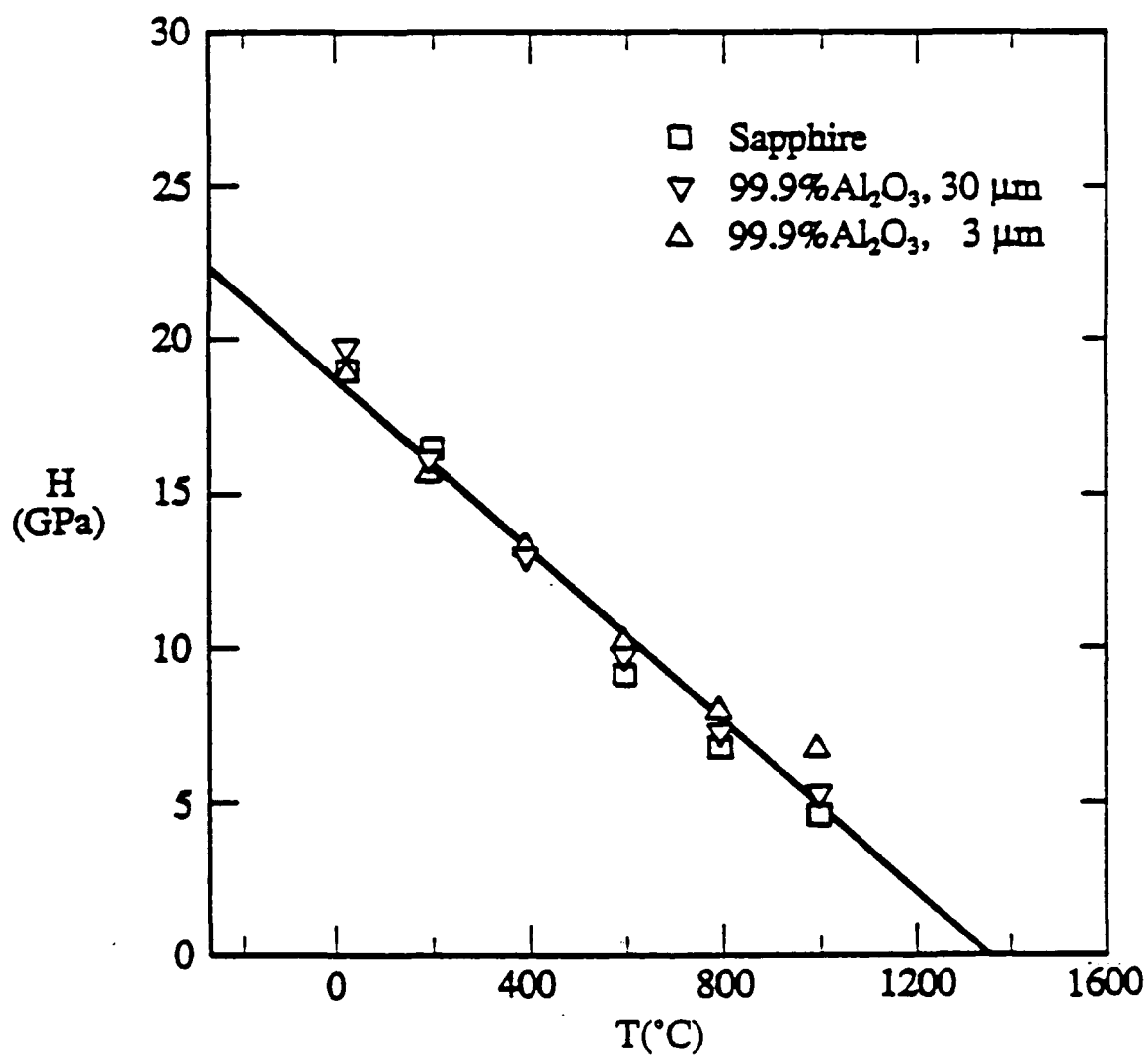


Figure 1. Hardness versus temperature for high-purity alumina of various grain size [9].

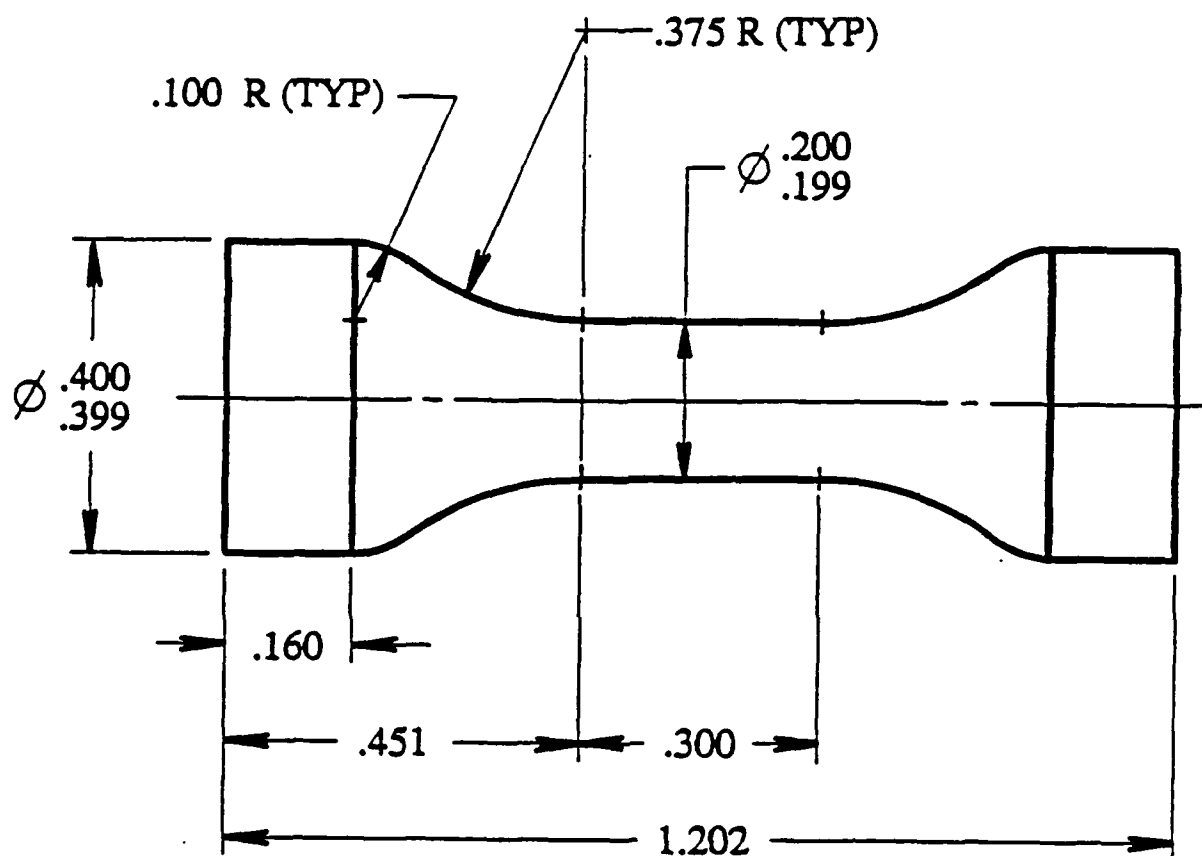


Figure 2. Current optimum (MTL) compression test specimen design [1].

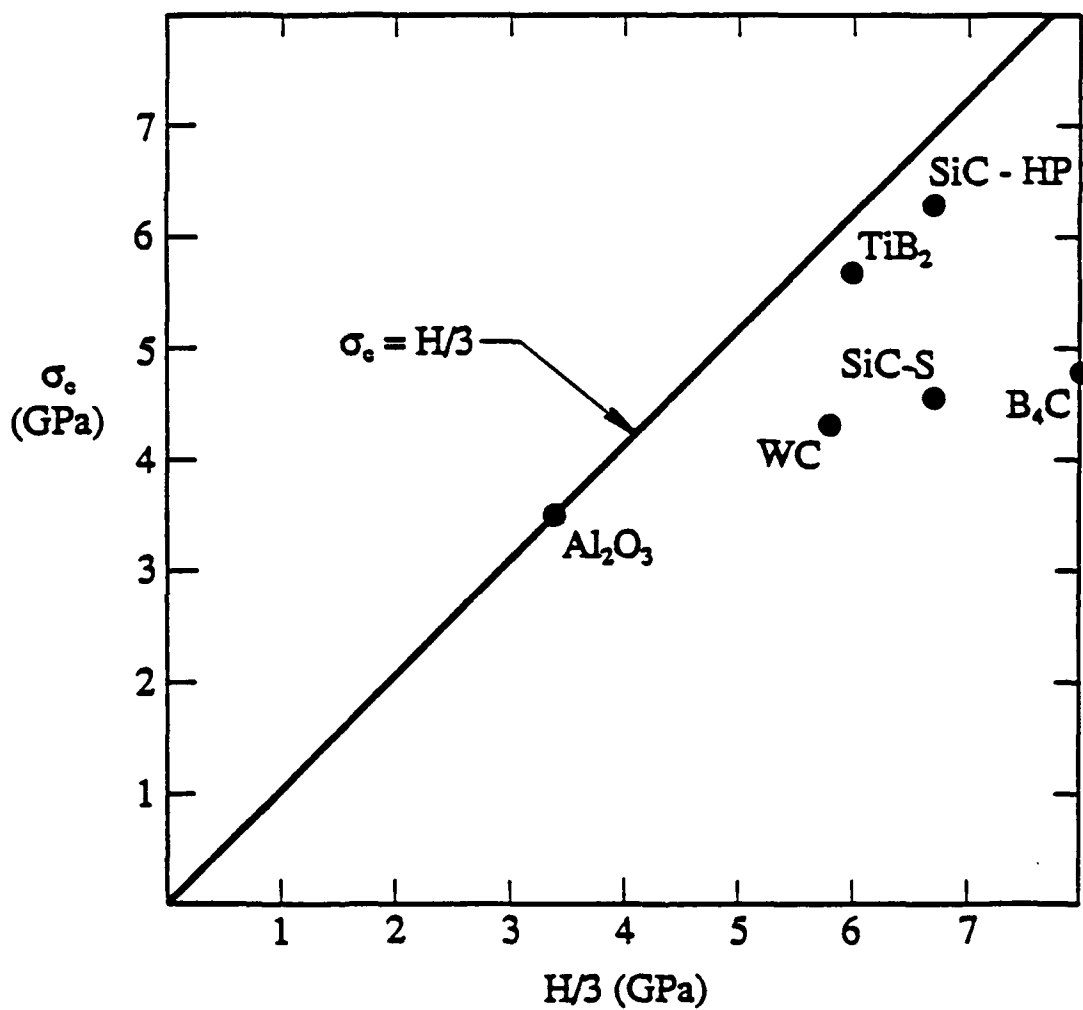


Figure 3. Compressive failure stress versus theoretical yield strength for strong ceramics using optimal uniaxial test configuration [1].

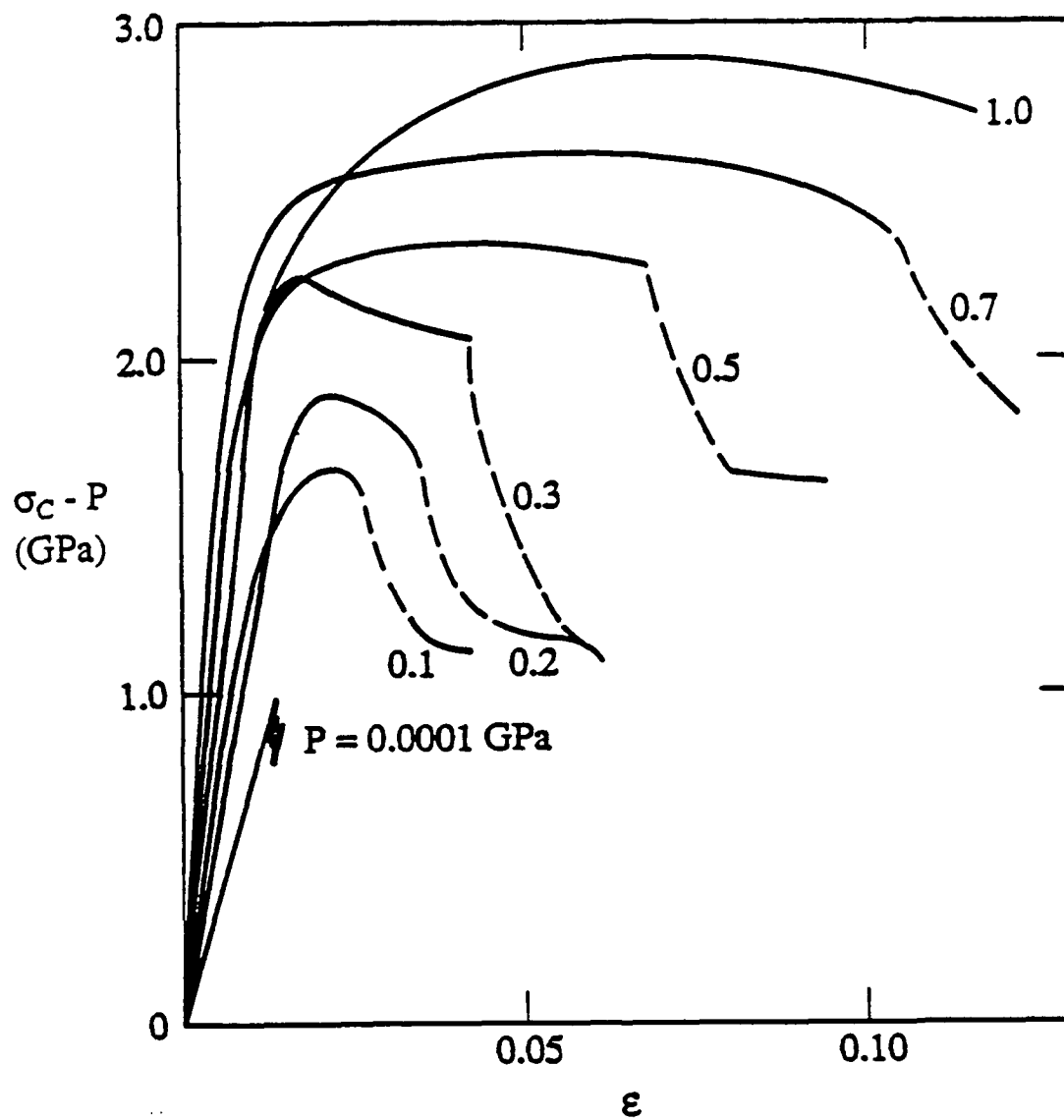
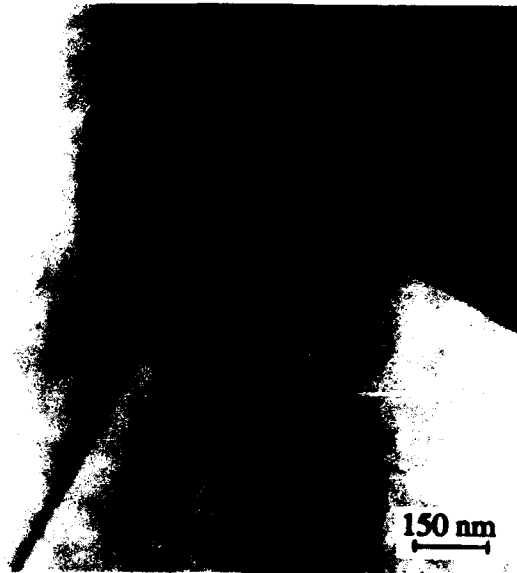
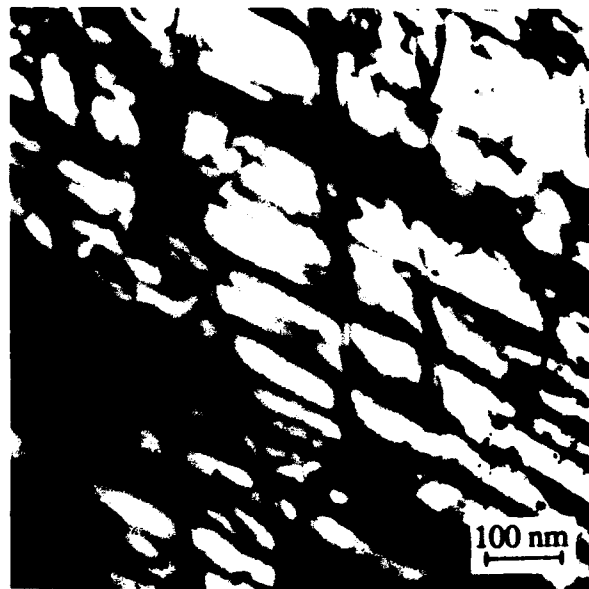


Figure 4. Compressive stress-strain curves for hot-pressed BeO; strain rate approximately $5 \times 10^{-5} \text{ s}^{-1}$. Numbers on curves denote confining pressure in GPa [32].



(a) Three grains from undeformed AlN. Initial dislocation density is very low; contrast with (b).



AlN grain from aggregates deformed at 0.7 GPa. Plane of photomicrograph is (0001); note traces of dislocation structures parallel to all three a-axes.

Figure 5. Transmission electron microscopy of aluminum nitride [32] (Courtesy of C. F. Cline).

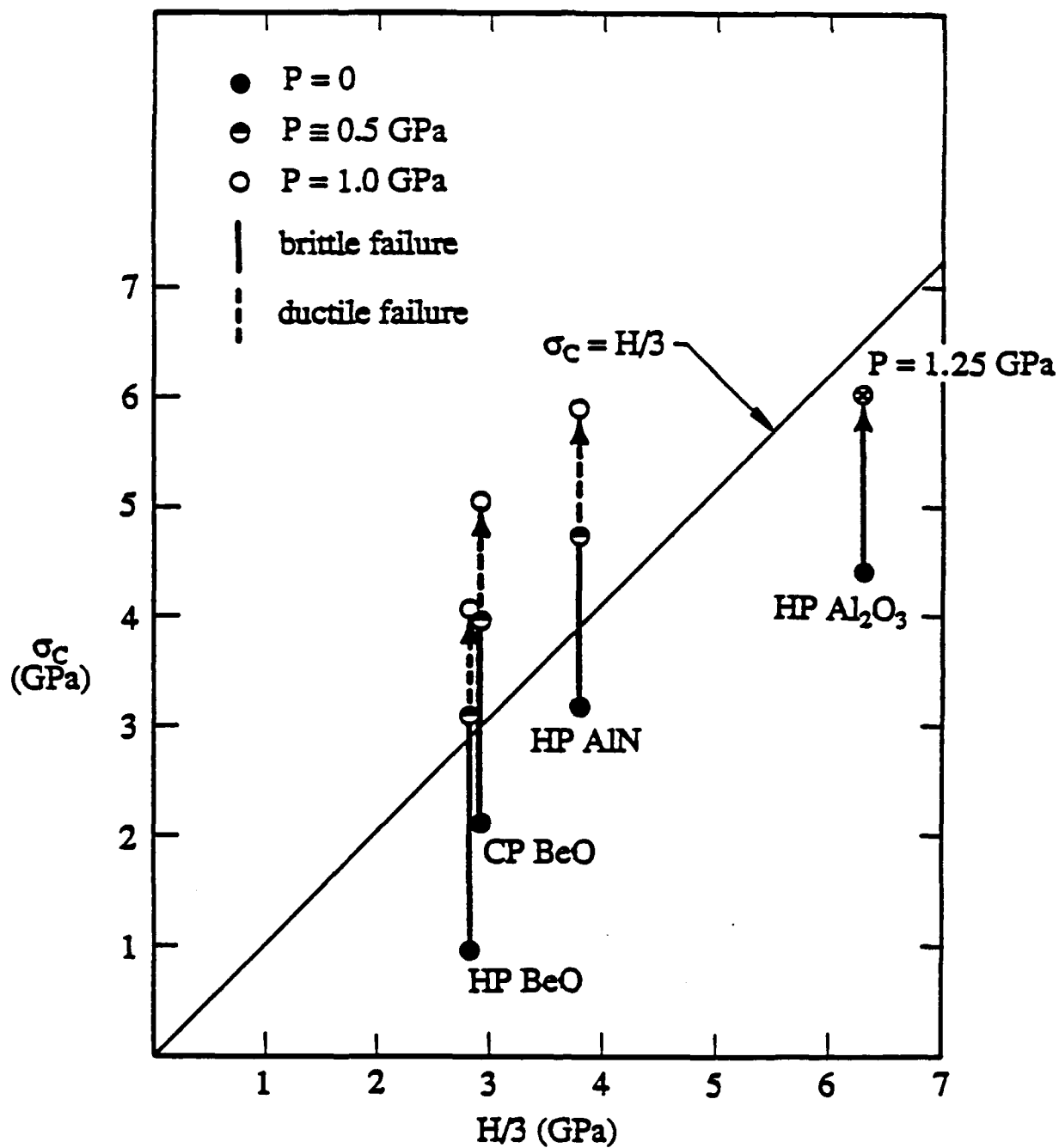


Figure 6. Compressive failure stress versus theoretical yield strength for strong ceramics tested under confining pressure [32].

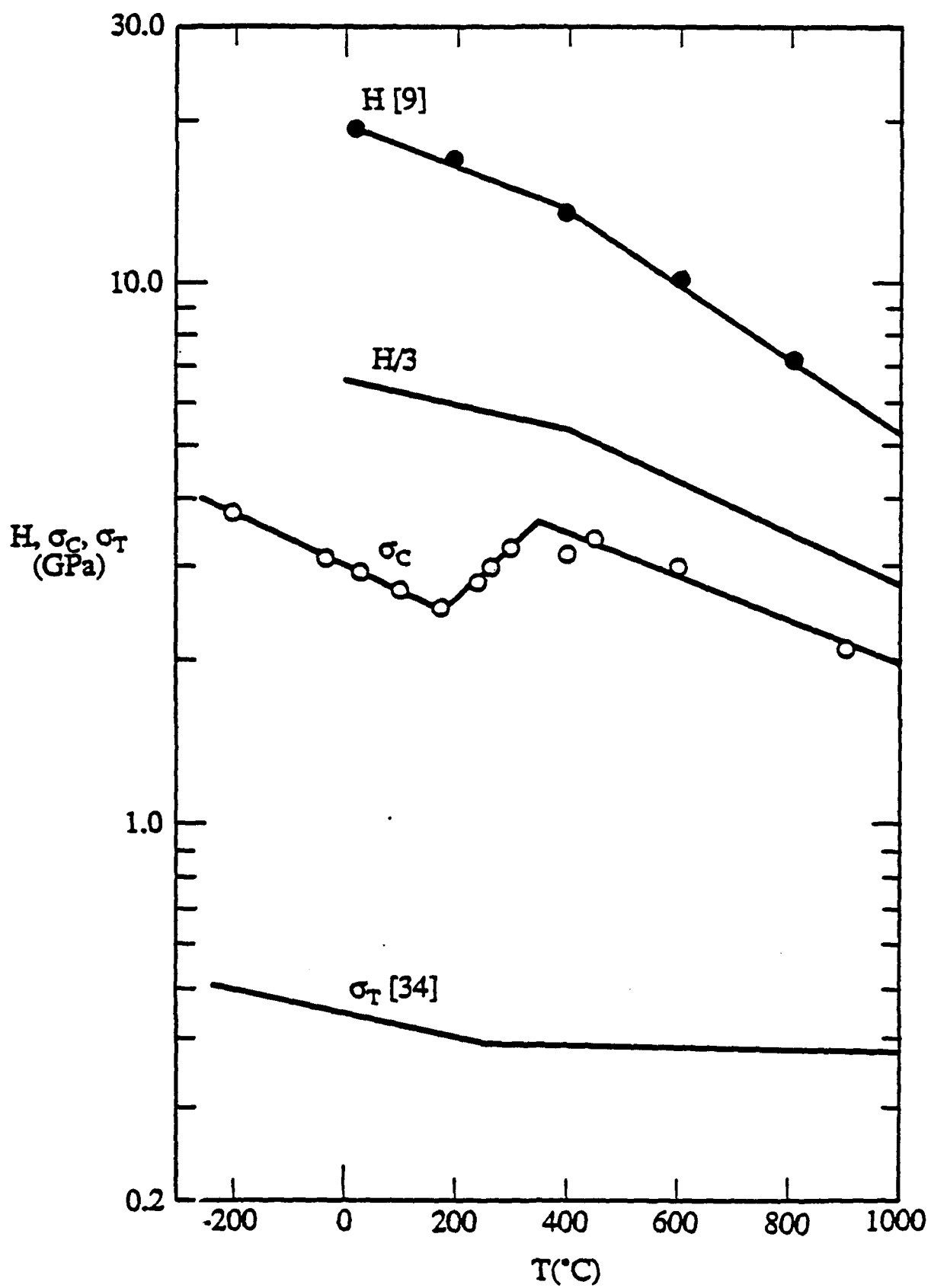


Figure 7. Hardness, theoretical yield strength, compressive failure stress, and tensile (bend) strength for coarse-grained ($\sim 30 \mu\text{m}$) 99.9% Al_2O_3 .

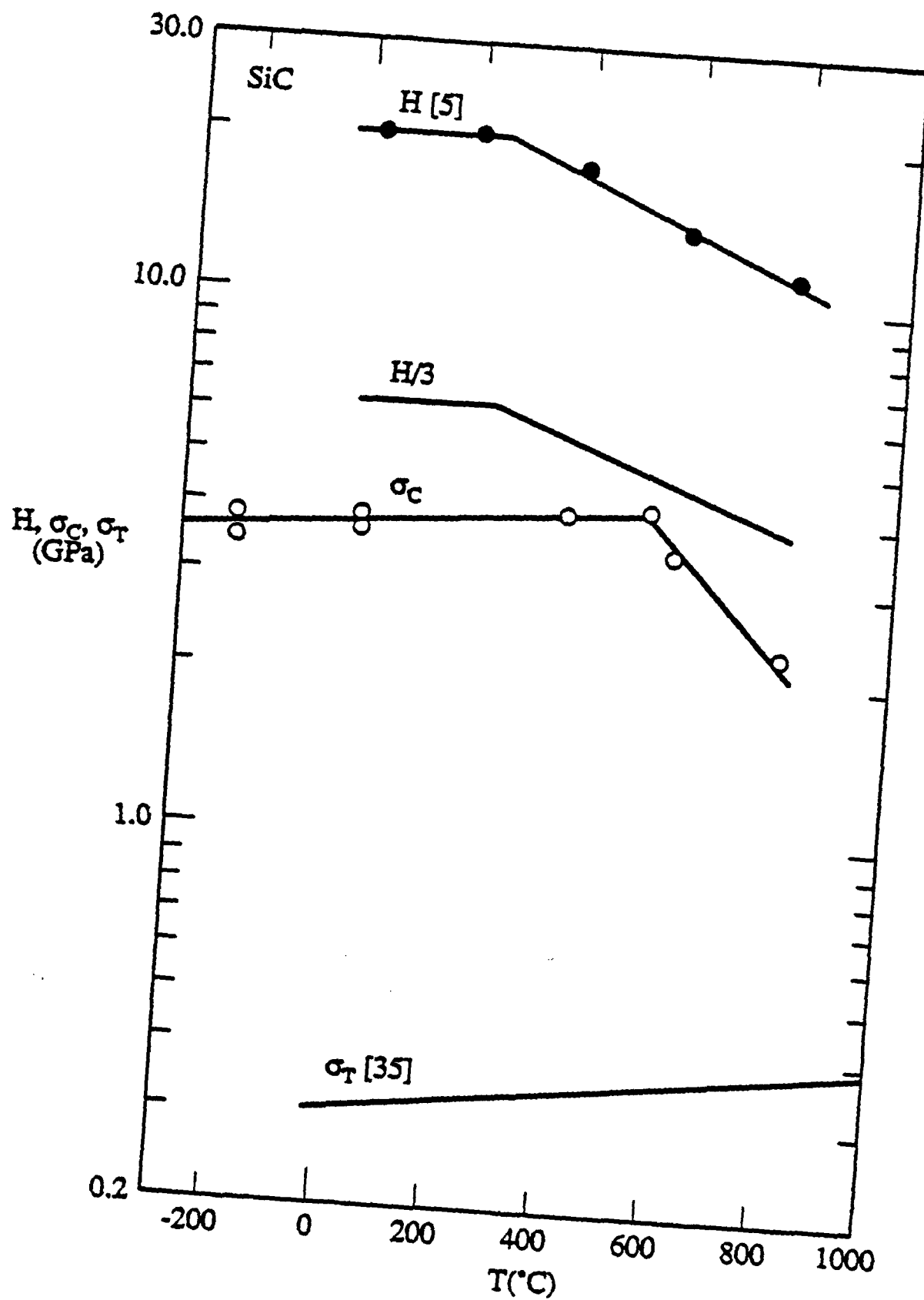


Figure 8. Hardness, theoretical yield strength, compressive failure stress, and tensile (bend) strength for fine-grained ($\sim 4 \mu\text{m}$) sintered alpha silicon carbide.

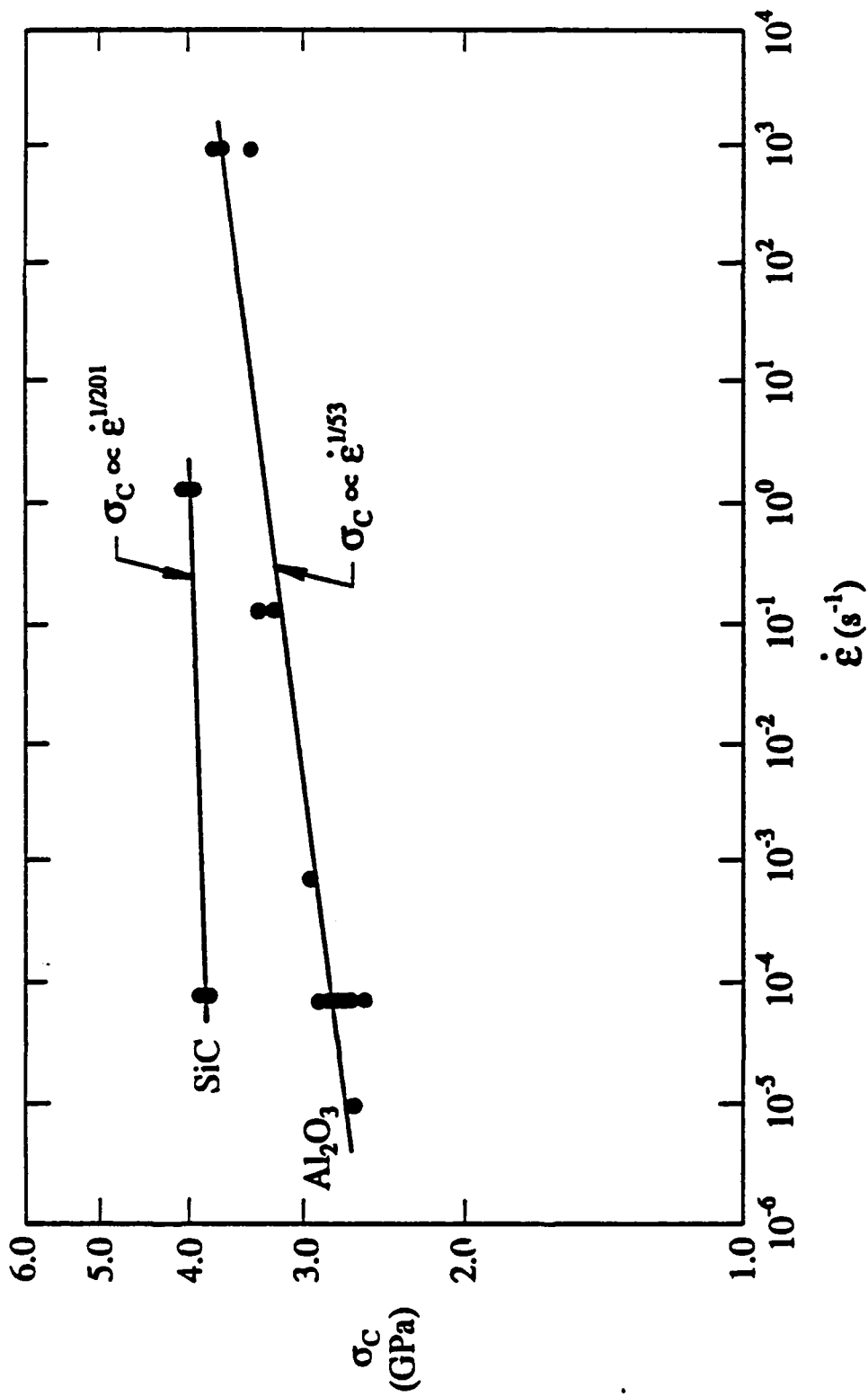


Figure 9. Compressive failure stress versus strain rate for coarse-grained high-purity alumina and fine-grained sintered alpha silicon carbide.

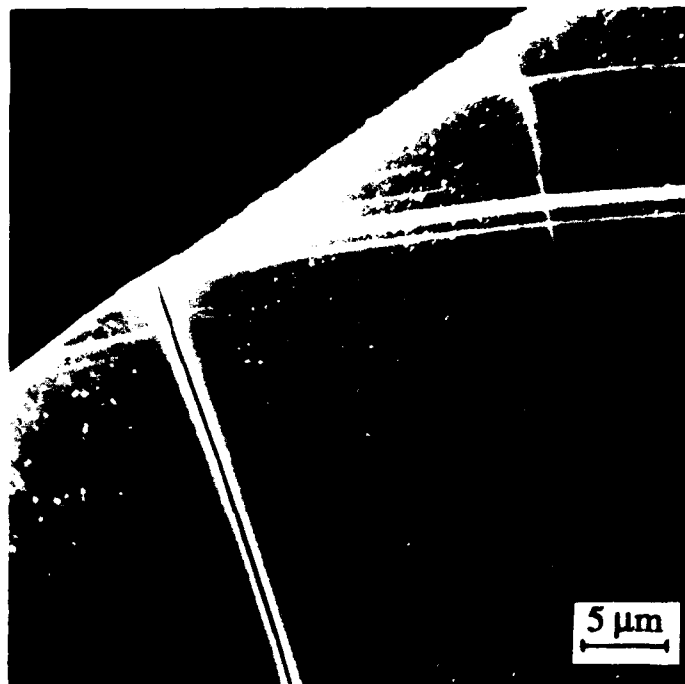


Figure 10. Axial microcracks nucleated by twin/deformation band interactions with grain boundary, Al₂O₃, T = 23°C.

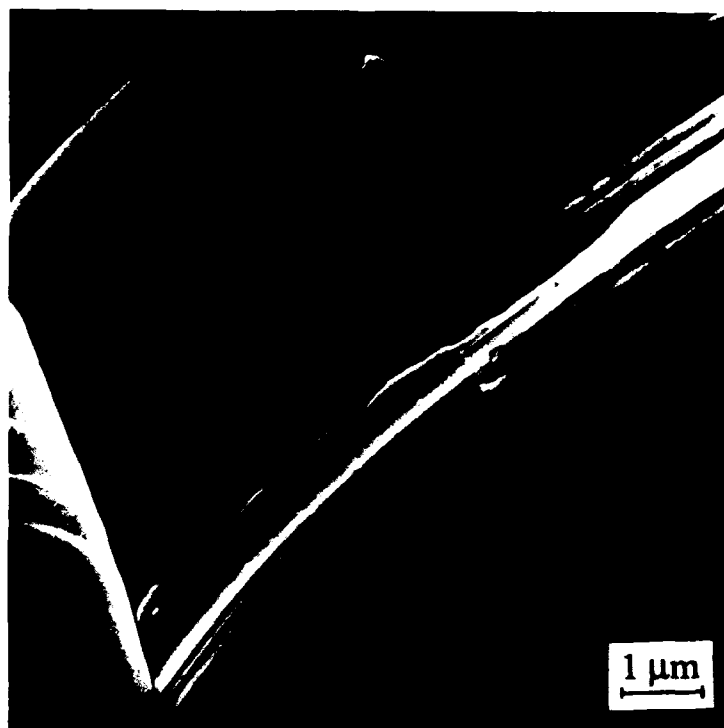


Figure 11. High magnification view of early stages of craze breakdown via void nucleation to form shear crack; $\dot{\epsilon} \cong 4000\text{s}^{-1}$, $\sigma \cong 0.92 \sigma_c$; compressive axis vertical.

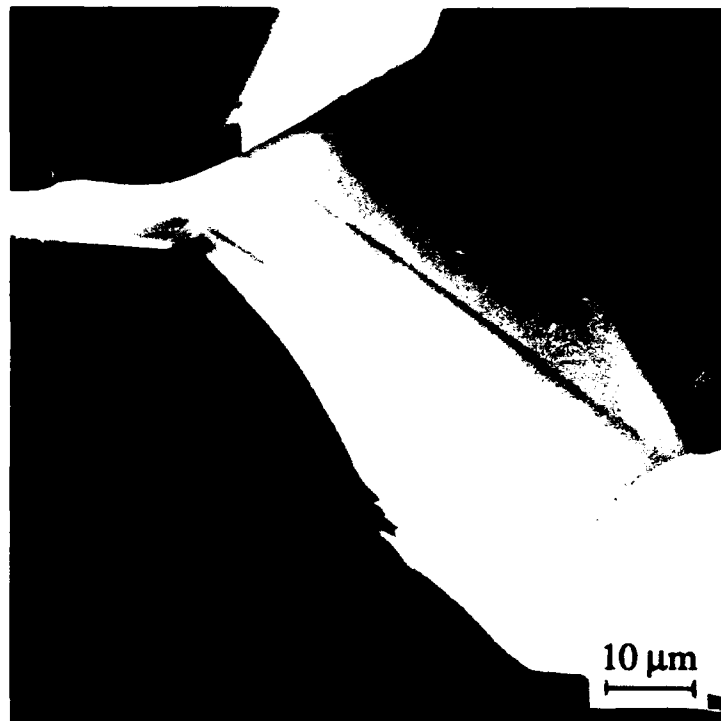


Figure 12. Grain boundary microfracture in Al_2O_3 caused by multiple twin impingement at $T = 500^\circ\text{C}$.



Figure 13. Dislocation slip bands (SB) in ∞ - SiC induced by compression at $T = 500^\circ\text{C}$. Slip appears to have caused GB cracking at A and B and slip band cracking at C. The bands appear to initiate at GB pores.

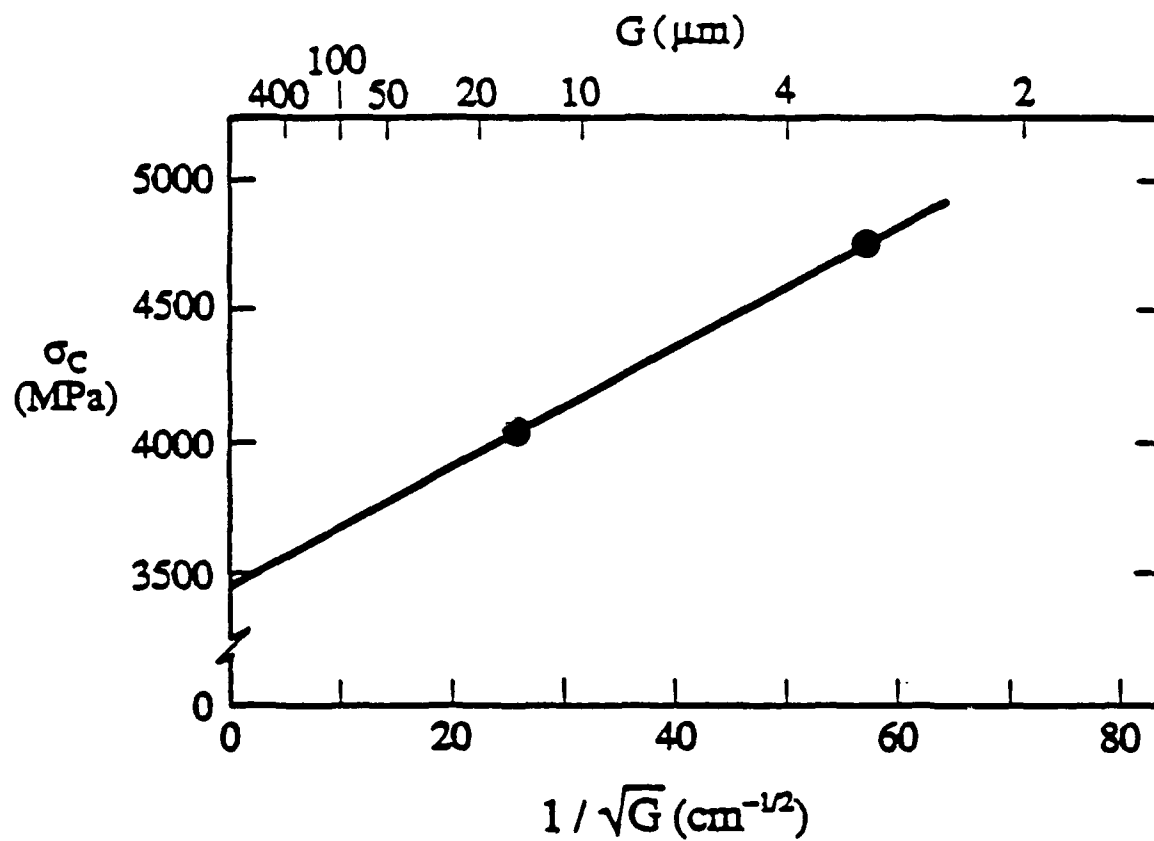


Figure 14. Compressive strength versus inverse square root grain size of near-theoretical density high-purity Al_2O_3 [2].

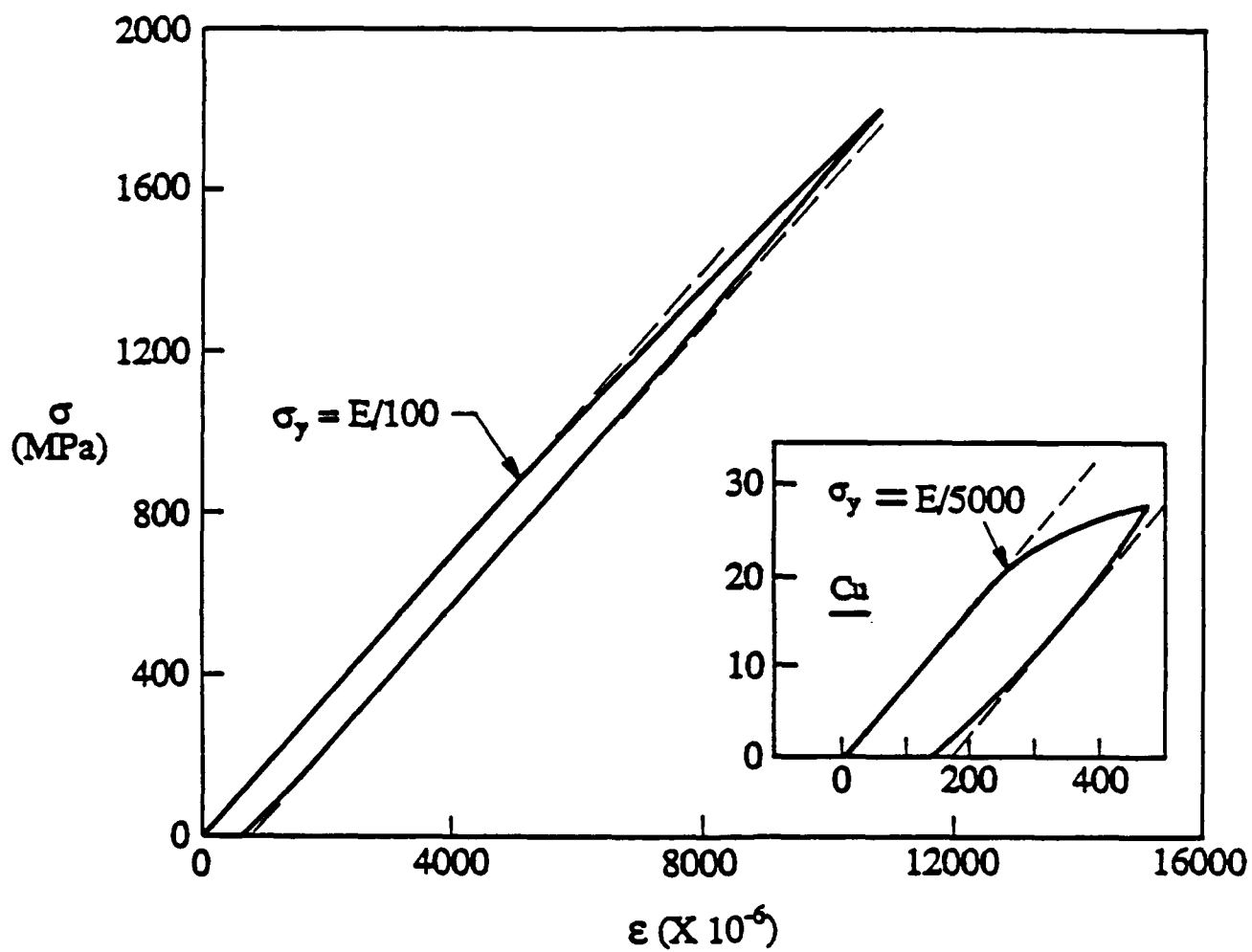


Figure 15. Stress-microstrain during compressive load-unload for fully stabilized ZrO_2 (inset shows data for polycrystalline Cu [50]).

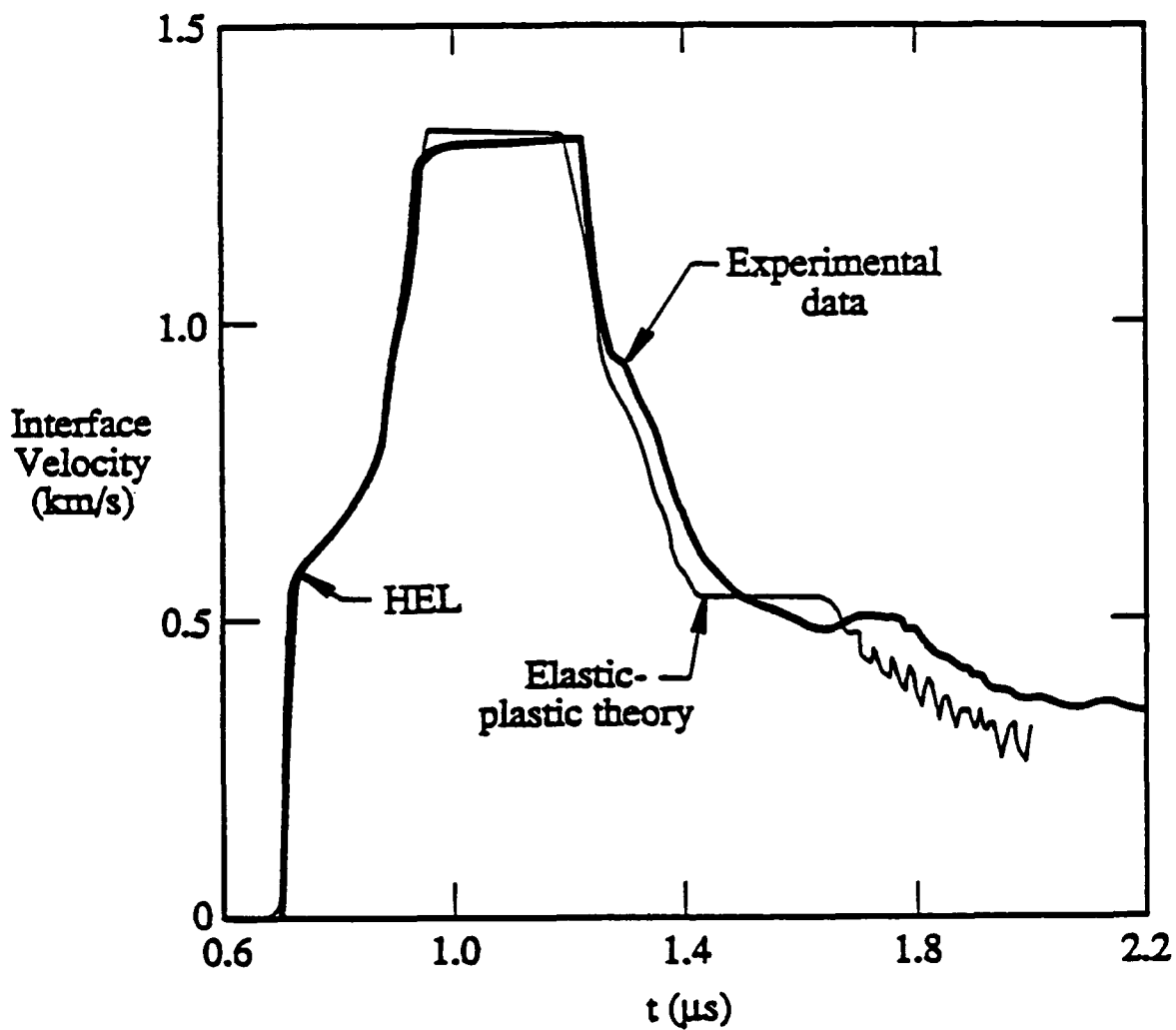


Figure 16. Silicon carbide flyer plate experiment and prediction by one-dimensional Lagrangian shock wave propagation code incorporating elastic-plastic hardening constitutive behavior [56].

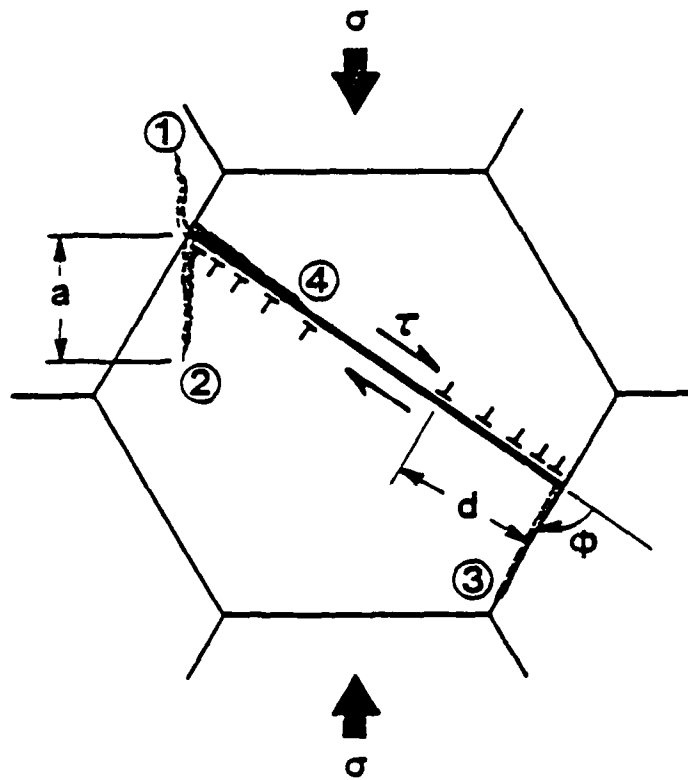


Figure 17. Geometry of compressive slip band-nucleated intracrystalline cleavage (1,2), intergranular separation (3), and slip band microfracture (4).

APPENDIX

Indentation - Derived Yield Strength

The fact that elastic strains may contribute significantly to the deformation associated with indentations was first recognized by Marsh [59], who was endeavoring to understand the behavior of glass. Based on his experiments, Marsh determined empirically that for high values of $\frac{E}{Y}$ (high modulus or low yield strength),

$$\frac{H}{Y} \equiv C \equiv 3 \quad (A1)$$

However, for situations in which $\frac{E}{Y}$ was lower, as for glass and polymers with their low elastic modulus, C was observed to be considerably smaller.

Johnson [60] subsequently analyzed the elastic-plastic stress field associated with an indentation, assuming isotropic yielding according to the von Mises criterion. He found that

$$C = \frac{2}{3} \left[1 + \ln \left(\frac{1}{3} \frac{E}{Y} \tan \beta \right) \right] \quad (A2)$$

where β is the angle between the indenter and the test surface. As $\frac{E}{Y}$ increases, the elastic strain during indentation decreases relative to the plastic response, so that C approaches 3 in the limit. Similarly, for low $\frac{E}{Y}$, C approaches the elastic limit, 1.1; this scenario is sketched in Figure A1, after Evans and Goetze [7].

In Figure A2, the Johnson relationship has been used [7] to compute the constraint constant versus temperature for pure Al_2O_3 (SiC behaves similarly). The graph is generated by iterating in Y at various temperatures for experimentally measured values of $H(T)$ and $E(T)$ in the equation

$$\frac{H(T)}{Y} \equiv C = \frac{2}{3} \left[1 + \ln \left(\frac{1}{3} \frac{E(T)}{Y} \tan \beta \right) \right] \quad (A3)$$

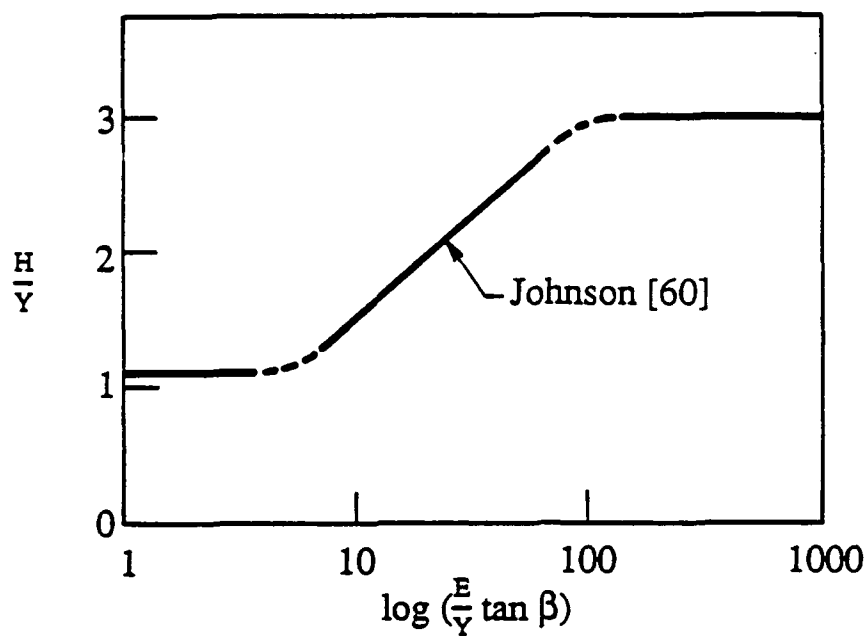


Figure A1. Correlation of the constraint constant with elastic-plastic theory [60].

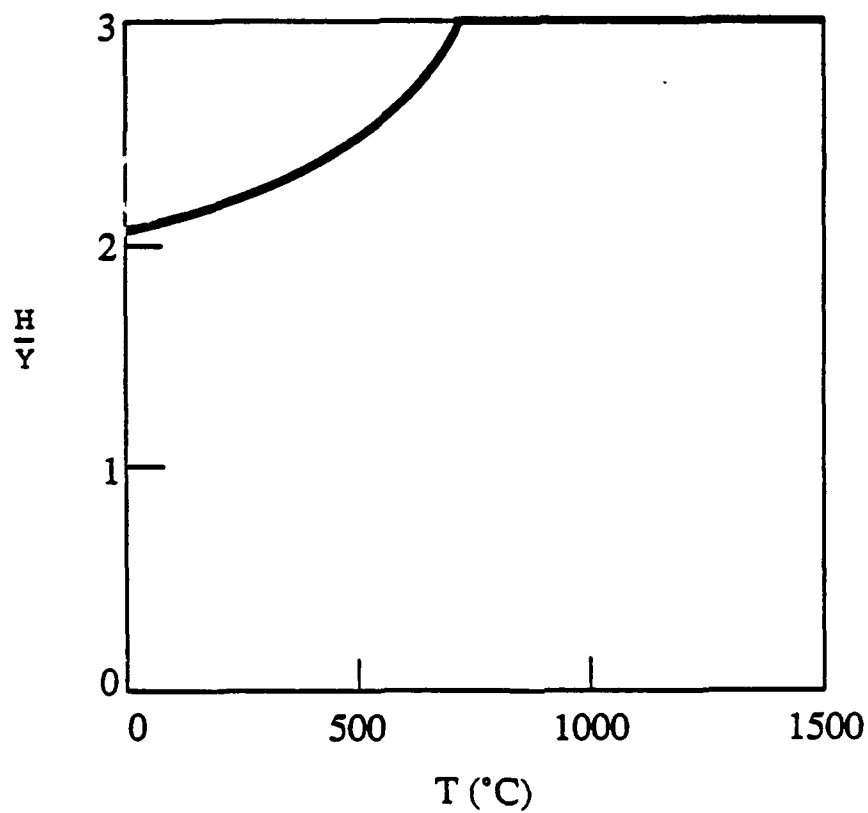


Figure A2. Computation of the constraint constant versus temperature for alumina [7] according to the theory of Johnson [60].

Based on this calculation, the ambient value of C for alumina should be approximately 2.1, somewhat lower than the plastic limit of about 3.0.

It should be noted that the validity of this theory has not been established for hard ceramics. Plastic deformation of these materials almost certainly is not isotropic, they may not obey von Mises, and elastic strains are much smaller than for glasses. The relatively low value of $\frac{E}{Y}$ for these materials derives from their high yield strength, but it is perfectly apparent that from a physical (observational) point of view, extensive plastic flow nevertheless occurs during the indentation of strong ceramics. Moreover, the compressive strength-under-confinement experiments of Heard and Cline [32] (discussed in the text) support the idea that C for such materials may be closer to 3 than would be predicted by Equation A3.

**Micromechanisms of Compressive Failure in a
Glass Fiber-Reinforced Amorphous Thermoplastic**

J. Lankford

Materials and Mechanics Department

Southwest Research Institute

6220 Culebra Road

San Antonio, Texas 78228-0510

ABSTRACT *Compressive failure of a 0°/90° glass fiber-reinforced amorphous thermoplastic is characterized. It is found that the critical event is the nucleation within 90° laminates of multiple shear crazes, which become shear microcracks, transition to axial cracks, and permit the specimen to fail by the flexure of 0° elements. Further, it is shown that the apparent kinetics of this process provide a rationale for the dramatic strain rate strengthening of these composites at high loading rate.*

INTRODUCTION

In a recent study,¹ the compressive behavior of a unidirectional PAN-derived carbon fiber-reinforced semicrystalline thermoplastic was characterized. Results obtained contrasted with those associated with earlier work^{2,3} involving thermoset-matrix composites. It was found, for example, that the thermoplastic-based composites yield well below failure, and that the latter occurs, with no precursory acoustic emission, via the sudden nucleation and propagation across the specimen of an unstable kink shear band. Further, it was determined that at high loading rates, the kinetics of kink propagation appeared to be responsible for a dramatic increase in strength, i.e., strain rate hardening. Finally, it was noted that the matrix accommodated the formation of kinks by local yielding; the matrix itself did not fail by microfracture or microvoid formation until late in the development of a macroscopic shear band.

Ongoing work has as its objective the assessment of the influence of composite composition and architecture on the compressive failure process. To that end, the present paper reports on the compressive behavior of an amorphous thermoplastic reinforced with glass fibers laid up in 0°/90° laminates. It will be seen that the results offer both similarities and contrasts with regard to the preceding findings.

MATERIAL

The particular composite chosen for study was an amorphous polyimide copolymer* reinforced with 15 μm diameter E-glass fibers. A polyetheretherketone (PEEK) derivative, the matrix has a low density (1.15 g/cc) and a melt laminate processing temperature of approximately 300°C.⁴ Unidirectional laminates of thickness on the order of 150 μm were laid up in a 0°/90° arrangement; laminates were composed of 60 volume percent fibers. The elastic modulus for the fibers was 75 GPa,⁵ while that of the matrix was only 3.2 GPa.⁴ Final void content of the composites was less than 1%.

* J-2, E. I. DuPont De Nemours, Inc., Wilmington, DE.

EXPERIMENTAL APPROACH

Design and verification of the compression test configuration has been detailed elsewhere. In particular, it was shown¹ that the cylindrically symmetric design (required for testing in a split Hopkinson pressure bar apparatus) yields quasistatic compressive strengths and evidences failure mechanisms essentially identical to those obtained in standard flat panel specimen configurations.^{6,7} The internally chamfered rings around the bases of the specimen were made of high strength steel, honed to a snug fit. All specimens, as well as matching hardened steel load platens, were carefully machined so that mating surfaces were parallel within 4 μm over the load surface diameter.

Using a standard servo controlled hydraulic machine, compression experiments were performed at strain rates ($\dot{\epsilon}$) ranging from $5 \times 10^{-6} \text{s}^{-1}$ to 5s^{-1} . For $\dot{\epsilon} \leq 10^{-4} \text{s}^{-1}$, acoustic emission (AE) was monitored using a transducer resonant at 160 kHz, with a filter-limited range of 100 kHz to 1 MHz. Earlier work^{8,9} has shown that this frequency regime corresponds to that of stress wave emission for microfracture in brittle materials such as ceramics.

Higher strain rates were achieved using the split Hopkinson pressure bar (SHPB) apparatus alluded to earlier. In particular, the latter experiments corresponded to $10^3 \text{s}^{-1} \leq \dot{\epsilon} < 10^4 \text{s}^{-1}$. Generally, such tests result in total failure of the sample; however, by reducing the incident projectile velocity slightly, it was possible to damage without failing some of the specimens.

These, and other samples loaded quasistatically to various damage levels, were sectioned and examined by optical and scanning electron microscopy (SEM). Specimens for SEM study were vapor deposited with gold, and imaged at low accelerating voltage to preclude electron beam damage of the polymeric component.

RESULTS

Shown in Figure 2 is a typical stress-strain ($\sigma - \epsilon$) curve generated at a strain rate of $6 \times 10^{-6} \text{ s}^{-1}$. Such results were obtained for all tests performed in the hydraulic machine, while the SHPB is incapable of discriminating the gradual, low level yielding shown in the figure; thus the latter test provided ultimate stress data only.

Also plotted in Figure 2 is the cumulative acoustic emission associated with damage development in the composite. It is evident that the threshold stress level for acoustic emission (σ_{AE}) is considerably in excess of the yield strength (σ_y). On the other hand, σ_{AE} is well below the ultimate strength (σ_c), indicating that the failure process is non-catastrophic, and probably requires the attainment of some critical state of damage.

Data for all specimens tested are summarized in Figure 3. For strain rates below about 100 s^{-1} , ultimate strength increases gradually with strain rate, a trend which is paralleled by that of σ_y and σ_{AE} . However, for $\dot{\epsilon} > 100 \text{ s}^{-1}$, there ensues a rapid increase in σ_c with $\dot{\epsilon}$; analysis of the latter results shows that within this regime, $\sigma_c \propto \dot{\epsilon}$.

Specimens tested under quasistatic conditions to the point of failure are characterized by the formation of a major shear plane, preceded by axial splitting, as shown in Figure 4. Closer inspection (Figure 5) shows that the splitting is isolated within the 90° laminates, and proceeds by growing around the periphery of near-adjoining glass fibers and through the intervening matrix.

Although these macroscopic cracks are axially oriented, their early stages of development are dominated by shear. In particular, they seem to nucleate near 90° fiber-matrix interfaces (Figure 6a), and apparently correspond to the breakdown of craze zones (Figure 6b). Clusters of these craze zones eventually link (Figure 7) to form an embryonic macrocrack, whose subsequent growth is axial. While the fiber-matrix interface is a critical factor in crack initiation, it is clear that the fiber-matrix bond strength is appreciable; one notes failed matrix microligaments adhering to the fibers in Figures 6b and 7.

Failure under more rapid loading conditions takes place according to a modification of this scenario. In particular, it can be seen (Figure 8) that if a high strain rate test is interrupted just prior to failure, the specimen will be characterized by an arrested "wave" of longitudinal splitting. In the figure, an untested specimen (left) is so oriented that the $0^\circ/90^\circ$ interfaces are parallel to the line of sight. After experiencing a dynamic load pulse, a similar specimen (right) has delaminated over nearly half its volume, the damage moving from left to right; apparently failure by macroscopic shear faulting does not occur until this sequential delamination process is complete. Closer inspection shows that the delamination process again occurs as for the quasistatic situation, i.e., within the 90° layers, with cracks running around the 90° fiber and across the matrix sectors which separate them. It should be noted that over the entire strain rate regime, delamination is somewhat of a misnomer. In point of fact, the 0° and 90° lamellae never fail at their original interfaces. Instead, cracking within the 90° components creates sheets consisting of 0° zones sandwiched between 90° surface layers.

Again, as for lower strain rates, dynamic crack nucleation is shear dominated. Figure 9 shows a region to the right of the arrested delamination wave of Figure 8; this precursory damage is oriented at roughly 45° to the load axis, and associated with fiber-matrix fracture and matrix shear cracking. One of the shear cracks has arrested (arrow, Figure 9) at a 0° fiber interface. Extensive study of 0° fiber bundles showed no intrinsic precursory damage or penetration by shear bands originating from 90° laminates.

At higher magnification (Figure 10a), the structure of the arrested shear crack is seen to be derived from an initial shear craze. Breakdown of the craze generally does not occur within the midplane, but rather at locations (arrows, Figure 10b) near the craze surface (i.e., the boundary with the parent matrix). In these photomicrographs, the structures shown represent local shear combined with Mode I (tensile) opening despite a nominal (vertical axis) pure compressive field. Clearly the latter is modified by the local response of the composite constituents.

The earliest observable (via SEM) stages of damage, i.e., located as far as possible to the right of, hence preceding, the arrested delamination "wave" in Figure 8, are shown in Figure 11. In this case, a shear craze has formed near a 90° fiber situated just outside the field of view in the lower right corner. The craze has grown toward the upper right, and has stopped just short of the 0° fiber at the left of the photo. Craze breakdown by a process of hole nucleation and coalescence has begun; the holes tend to nucleate near the craze surface, and by linking up will eventually produce the morphology shown in Figure 10.

DISCUSSION

The foregoing observations raise several issues, which will be considered in the following section. In particular, these include (1) the sequence of events leading to failure versus that shown earlier to be responsible for the failure of unidirectional graphite fiber-reinforced semi-crystalline PEEK, and (2) how this sequence might relate to the enhanced sensitivity of strength to strain rate under dynamic loading conditions.

Clearly, the critical event in the failure of these composites lies in the nucleation of shear microcrazes within the 90° laminates. This seems to occur (Figures 6 and 7) very close to certain fiber-matrix interfaces, suggesting that it is the stress gradient or enhancement at a strongly bonded interface which is responsible. Since subsequent craze growth takes place within shear planes, it appears that both shear and local tension (to drive the opening of the craze surfaces and induce fibril drawing) must exist within certain enclaves of interacting 90° fibers, despite the nominal global compressive stress field. Finite element analysis probably will be required to characterize such enclaves. At this point, however, it seems reasonable to associate σ_y with near-interface matrix yielding by crazing.

Breakdown of microcrazes to form shear microcracks probably begins at slightly higher stresses, but still below σ_{AE} . Since this process seems to be one involving void nucleation rather than microfracture, it would not be expected to generate stress wave emission.

This may not be true for the later stages of craze breakdown, however, Lauterwasser and Kramer¹⁰ have performed detailed studies of the (micro) fracture of crazes in thick sheets of polystyrene (PS) loaded in pure tension. In these experiments, it was found that once a mature craze has formed, it will start to fail by slowly growing an embryonic crack along its midrib, a highly drawn fibrillar (hence lower density) region running along the central plane of the craze. Quickly, however, the imposition of the stress field of the embedded crack begins to generate highly drawn craze fibrils very close to the craze surface, i.e., further drawing of the midrib is not observed. This preferential strain localization eventually creates a situation in which, in the view of Lauterwasser and Kramer, it is essentially more favorable for the crack to advance through the highly drawn new craze zone at the craze/solid boundary than to continue to grow along the midrib. The result is rapid material separation alternating from one surface of the craze to the other, as observed in the present study for both quasistatic (Figure 6b) and dynamic (Figure 10) loading rates. Since this type of failure is caused by rapid increments in crack extension, it may generate acoustic emission, hence could correspond to the global attainment of σ_{AE} .

Once a macroscopic crack has formed from the coalescence of a series of shear microcracks, there is a transition from shear to axial growth. This phase probably is facilitated by the tendency of hard fibers compressing relatively thin intervening matrix zones, to produce local tensile stresses normal to the compressive stress axis. Such stresses permit axial cracks to jump rapidly from one fiber to another, probably with significant acoustic emission. Under quasistatic conditions, this process may promote concurrent axial delamination throughout the specimen, while under dynamic loading, delamination once begun at a preferential near surface site proceeds across the sample in a fast wave. The speed of this wave will be controlled by craze nucleation/propagation kinetics.

At the point of basically complete delamination, the specimen still has not failed. Failure is reached shortly afterward, as delaminated layers flex outward, testing the tensile flaw distributions of the outermost glass fibers.¹¹ These finally fail in bending (local tension), transferring the load to the next layer; subsequent gross failure is essentially instantaneous.

Interestingly, the strength-strain rate dependence found for dynamic loading conditions is similar to that obtained earlier¹ for 0° graphite fiber-reinforced semicrystalline PEEK (Figure 12). In the latter case, failure is initiated by classic matrix deformation, which at certain sites permits the nucleation of kink bands within individual fibers. Failure ensues when several of these kink bands grow and intersect, or one of them grows all the way across the specimen. Since the time for failure depends on the kinetics of shear band propagation, it can be shown theoretically¹² that within the dynamic loading regime, $\sigma_c \propto \dot{\epsilon}^{1.0}$, a conclusion which was validated by the earlier experimental results.

In the present case, it is known¹¹ that E-glass fibers do not kink, but instead fail by the nucleation of tensile microcracks as the fibers flex. Thus, failure kinetics can be considered in terms of the following expression for the time to fail, i.e.,

$$t_f = \frac{l_1}{C_1} + \frac{Nl_2}{C_2} \quad (1)$$

where l_1 is the distance that a shear crack within a 90° laminate must grow at a shear velocity C_1 before transitioning to an axial crack, and l_2 is the distance that N of these axial cracks must grow at a velocity C_2 before flex/failure can occur. Since the strain rate at failure can be written

$$\dot{\epsilon} = \frac{\sigma_f}{Et_f} \quad (2)$$

where σ_f is the stress at failure and E the elastic modulus, substituting Equation 1 for t_f in Equation 2 yields

$$\sigma_f = E \left(\frac{l_1}{C_1} + \frac{Nl_2}{C_2} \right)^{-1} \dot{\epsilon} \quad (3)$$

or $\sigma_f \propto \dot{\epsilon}^{1.0}$. Thus, the same functional relationship is obtained as that established for the kink-prone unidirectional composite,¹ but deriving from a different physical process.

ACKNOWLEDGEMENTS

The meticulous experimental work of A. Nicholls is acknowledged with appreciation. Support of the Office of Naval Research through contract No. N00014-84-C-0213 is gratefully acknowledged.

REFERENCES

1. J. Lankford, "Compressive Damage and Failure at High Loading Rate in Graphite Fiber-Reinforced Polymeric Matrix Composites," *Advanced Composite Materials*, ed. M. D. Sacks, American Ceramic Society, Westerville, OH, 553-563, 1991.
2. C. Cazeneuve and J. -C. Maile, "Study of the Behavior of Carbon Fiber-Reinforced Composites at Different Rates of Deformation," *J. Physique*, **46**, 551-556, 1985.
3. P. Kumar, A. Garg, and B. D. Agarwal, "High Strain Rate Behavior of Unidirectional GFRP," *J. Aero. Soc. India*, **38**, 11-16, 1986.
4. W. H. Krueger, S. Khan, R. B. Croman, and I. Y. Chang, "High Performance Composites of J-2 Thermoplastic Matrix Reinforced with Kevlar Aramid Fiber," Proc. 33rd Int. SAMPE Sym., 181-193, 1988.
5. *Ceramic Source*, American Ceramic Society, **3**, 229, 1987.
6. N. R. Adsit, "Compression Testing of Graphite/Epoxy," *Compression Testing of Homogeneous Materials and Composites*, ASTM STP 808, ed. R. Chait and R. Papirno, American Society for Testing and Materials, Philadelphia, 175-186, 1983.
7. R. J. Lee, "Compression Strength of Aligned Carbon Fiber-Reinforced Thermoplastic Laminates," *Composites*, **18**, 35-39, 1987.
8. J. Lankford, "Tensile Failure of Unflawed Polycrystalline Al_2O_3 ," *Journal of Materials Science*, **11**, 351, 1978.

9. J. Lankford, "Temperature-Strain Rate Dependence of Compressive Strength and Damage Mechanisms in Aluminum Oxide," *Journal of Materials Science*, **16** 1567, 1981.
10. B. D. Lauterwasser and E. J. Kramer, "Microscopic Mechanisms and Mechanics of Craze Growth and Fracture," Materials Science Center Report 3076, Cornell University, August 1978.
11. H. T. Hahn and J. G. Williams, "Compression Failure Mechanisms in unidirectional Composites," Composite Materials: Testing and Design (Seventh Conference), ASTM STP 893, ed. J. M. Whitney, American Society for Testing and Materials, Philadelphia, 115-139, 1986.
12. J. Lankford, "Dynamic Compressive Fracture in Fiber-Reinforced Ceramic Matrix Composites," *Mats. Sci. Eng.*, **A107**, 261-268, 1989.

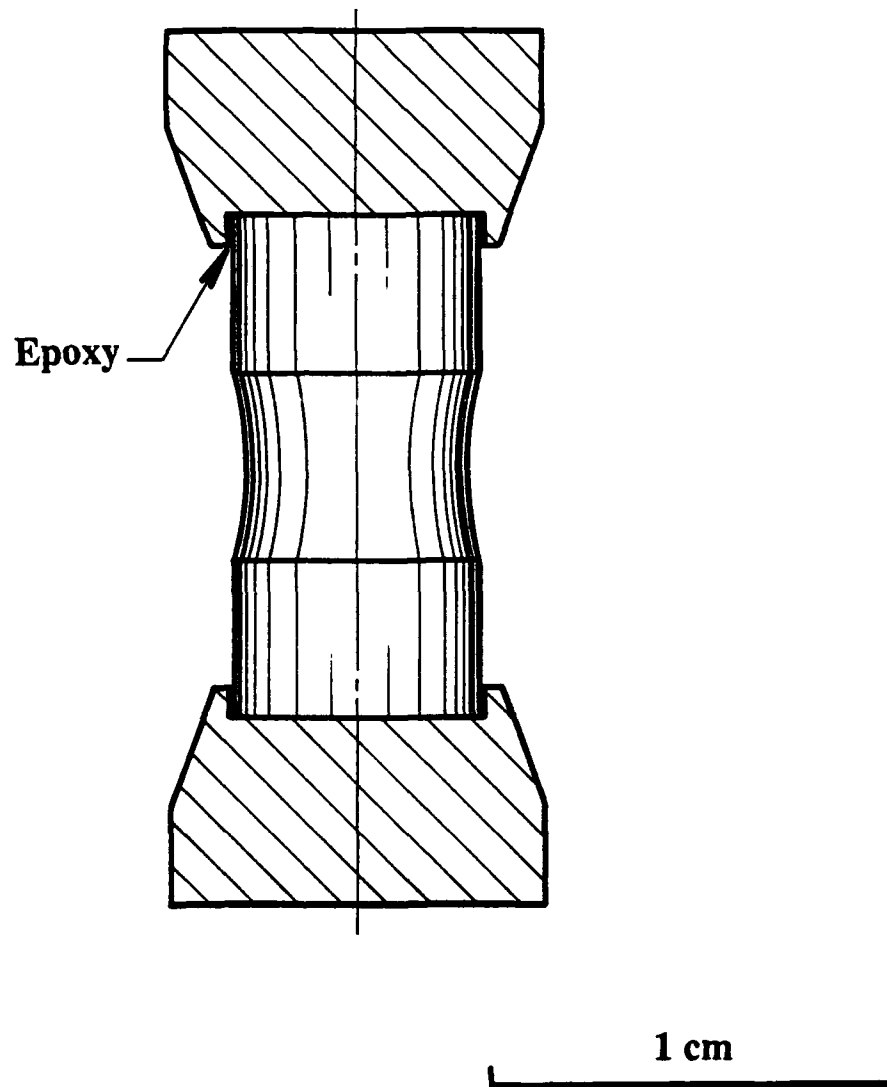


Figure 1. Configuration of compression test specimen.

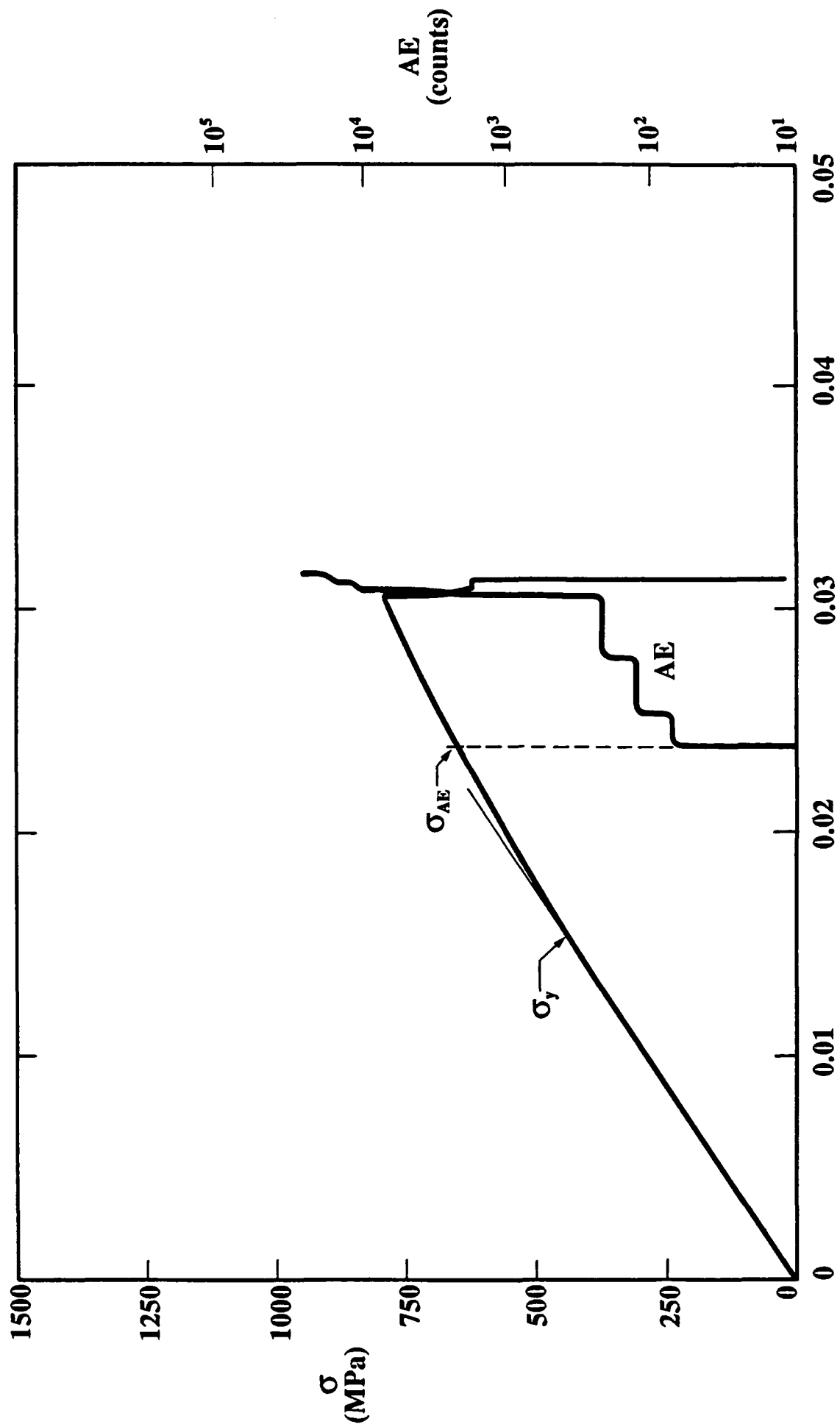


Figure 2. Compressive stress and acoustic emission versus strain, $\dot{\epsilon} = 6 \times 10^{-6} \text{ s}^{-1}$.

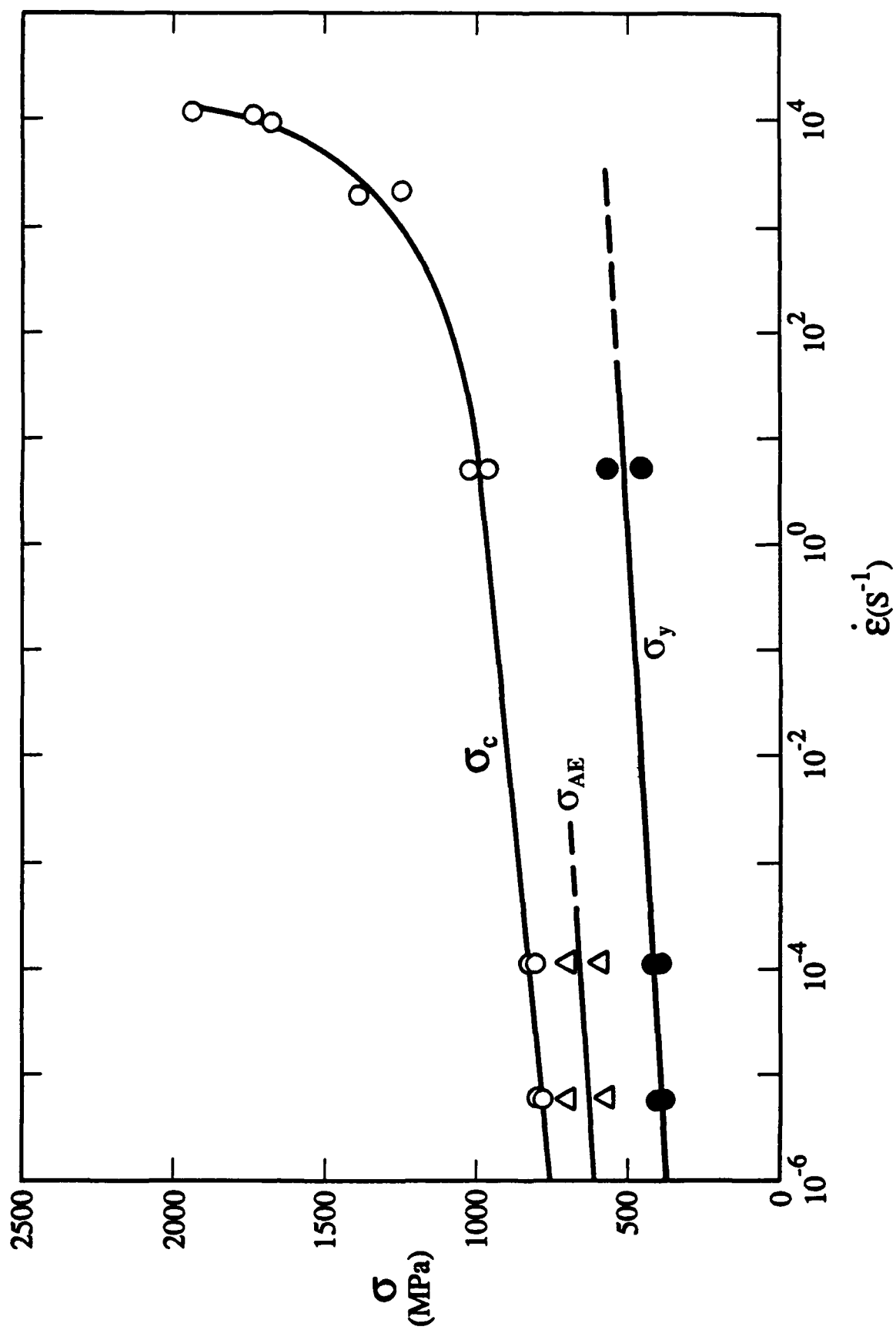
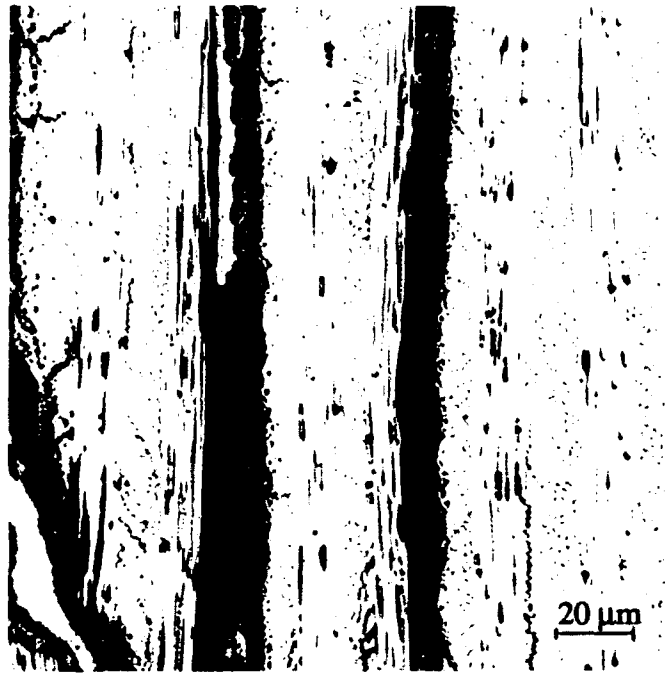


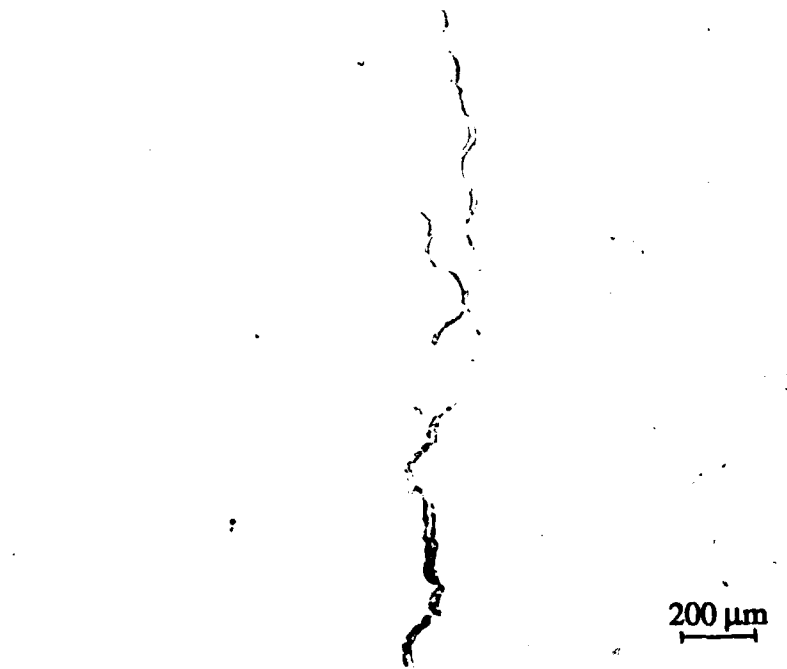
Figure 3. Stress level versus strain rate.



Figure 4. Macroscopic view of failed specimen, $\dot{\epsilon} = 1 \times 10^{-4} \text{s}^{-1}$, showing shear failure preceded by axial splitting.

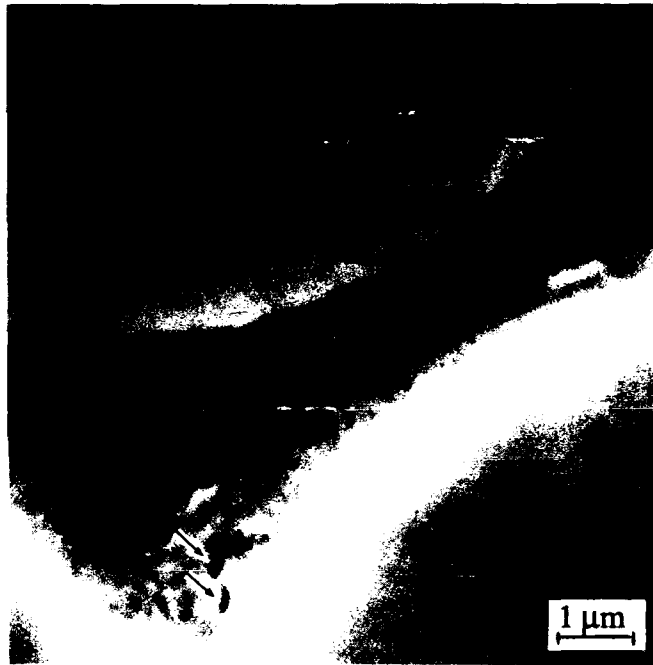


(a) Axial splitting.

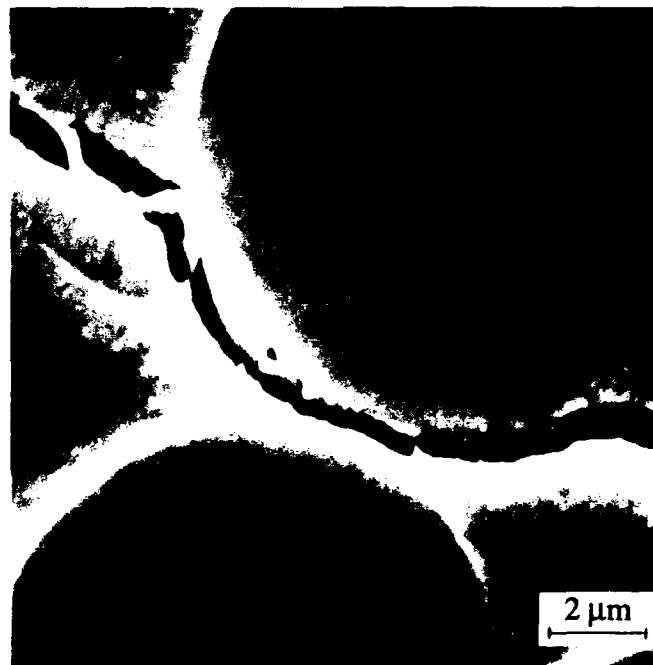


(b) Axial crack development within 90° laminates.

Figure 5. Axial damage development; $\dot{\epsilon} = 1 \times 10^{-4} \text{ s}^{-1}$, stress axis vertical, $\sigma = \sigma_c$.



(a) Microcrack initiation near fiber interface; void formation (arrows) within apparent matrix shear band.



(b) Transition of near-interface microcrack to shear-oriented craze crack.

Figure 6. Microcrack nucleation within 90° laminate;
 $\dot{\epsilon} = 1 \times 10^{-4} \text{ s}^{-1}$, stress axis vertical, $\sigma \cong 0.95 \sigma_C$.

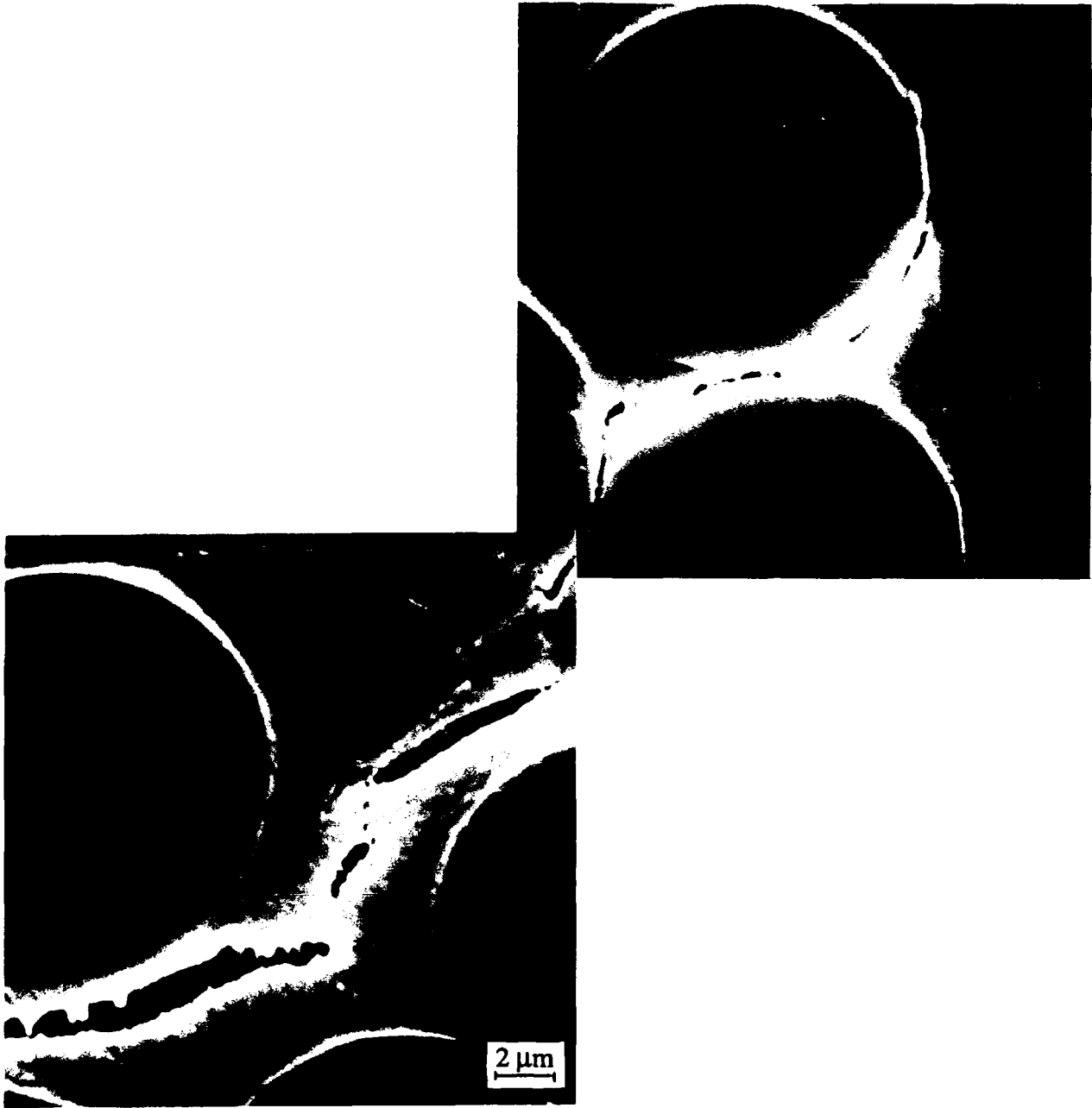


Figure 7. Linkup of shear microcracks within 90° laminate; $\dot{\epsilon} = 1 \times 10^{-4} \text{ s}^{-1}$, stress axis vertical, $\sigma \approx 0.95 \sigma_c$.

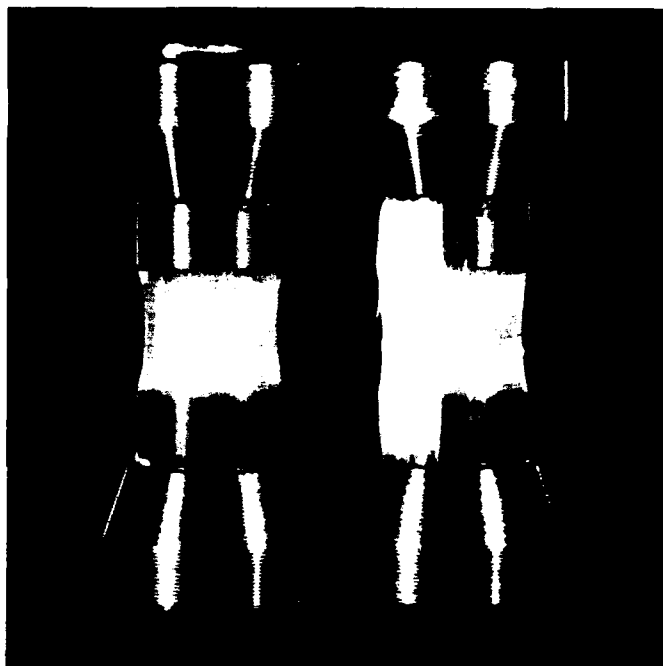


Figure 8. Untested specimen (left) versus sample (right) tested at $\dot{\epsilon} = 4000\text{s}^{-1}$ to a near failure stress level ($\sigma \cong 1500\text{ MPa}$).

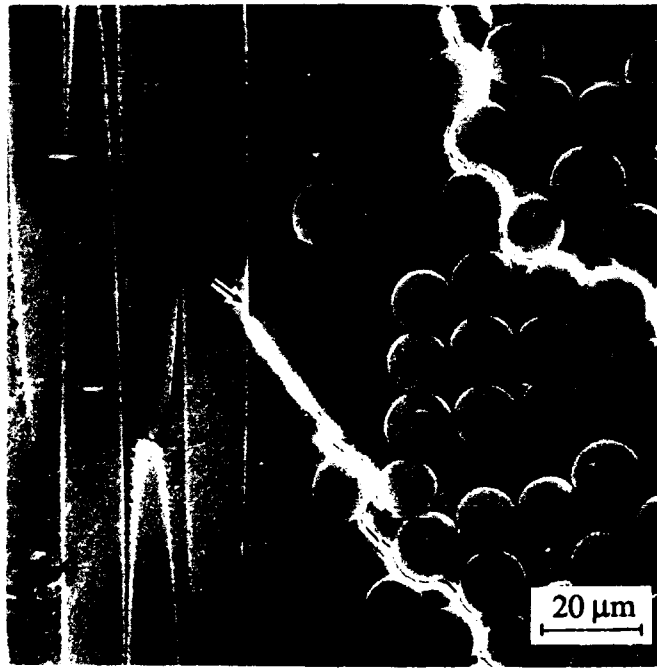
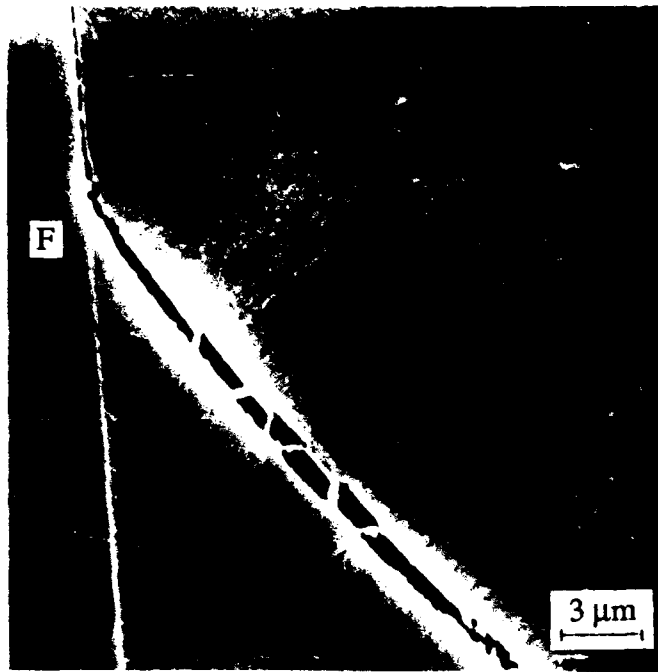
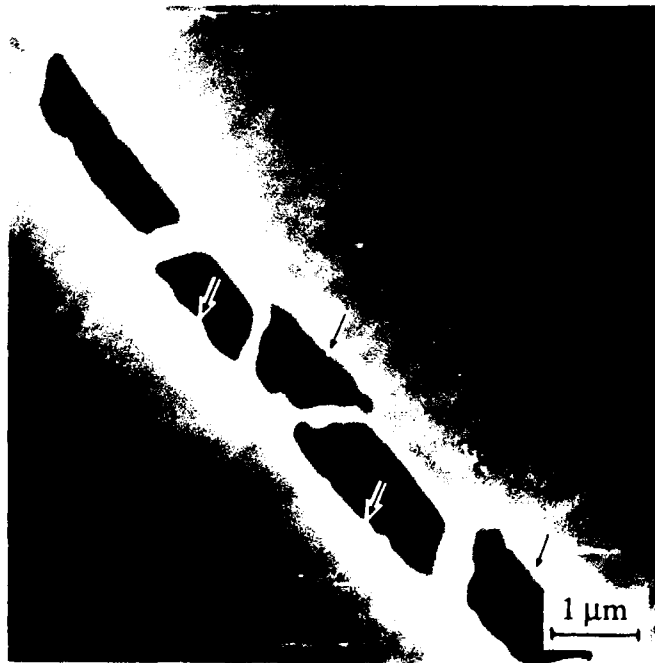


Figure 9. Dynamic shear crack nucleated in 90° laminate at $\dot{\epsilon} \cong 4000\text{s}^{-1}$, $\sigma \cong 0.92 \sigma_c$, compressive axis vertical; crack has arrested (arrow) at 0° fiber interface.



(a) Craze basis of shear band; craze arrest at 0° fiber interface (F).



(b) Evidence of craze breakdown at craze surface (arrows).

Figure 10. Details of shear band shown in Figure 9.



Figure 11. Twin habit plane/deformation band cracking, Al_2O_3 , $T = 23^\circ\text{C}$.

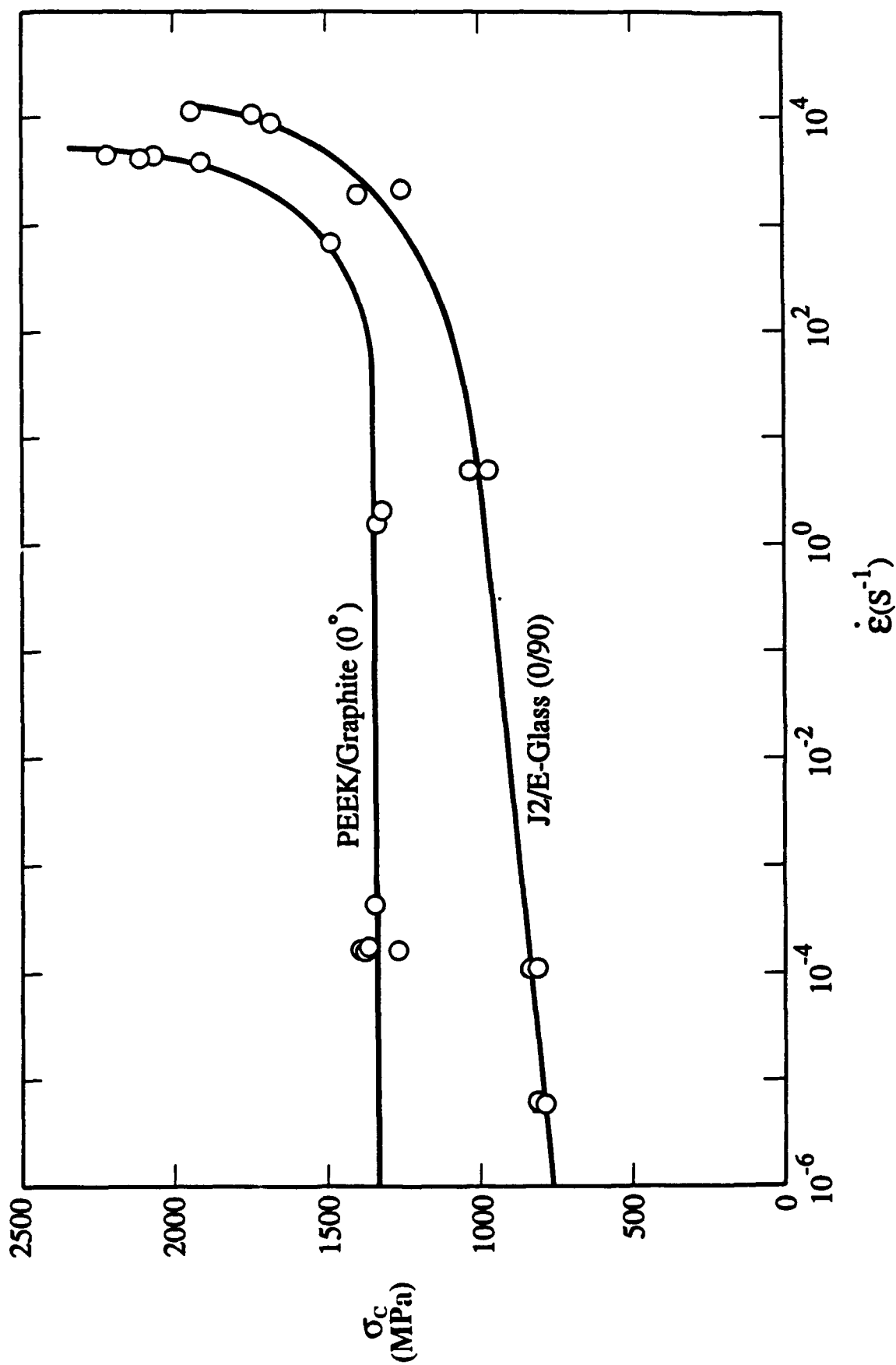


Figure 12. Compressive strength versus strain rate for unidirectionally graphite fiber reinforced semicrystalline PEEK versus $0^\circ/90^\circ$ glass fiber reinforced amorphous thermoplastic.